

# An Innovative, Adaptive Faulty Signal Rectifier Along with a Switching Controller for Reliable Primary Control of GC-VSIs in CPS-Based Modernized Microgrids

Masoud Davari <sup>✉</sup>, Senior Member, IEEE, Mohammad Pourmahmood Aghababa <sup>✉</sup>, Member, IEEE, Frede Blaabjerg <sup>✉</sup>, Fellow, IEEE, and Mehrdad Saif <sup>✉</sup>, Senior Member, IEEE

**Abstract**—Nowadays, networked controls using cyber-physical systems (CPSs) necessitate engineers considering “faulty signals” into the control from the beginning of the design process. Therefore, synthesizing control methods, which are able to deal with faulty signals and tolerate them, must be thoroughly investigated and integrated into the design process from the commencement. This article proposes an innovative, reliable control based on a sliding mode faulty signal rectifier for active-/reactive-power-controlled, grid-connected voltage-source inverters (named GC-VSIs hereinafter). It is called “faulty-signal-tolerant” control in this article. Those faulty signals can reach the GC-VSI’s controls from any sources; for example, they may arise provided that the CPSs malfunction or fail to prevent data-integrity-related issues, cyber threats, and more. The sliding mode algorithm provides the proposed controller with resilient performance via rectifying faulty signals. Besides, the proposed structure is enhanced by an adaptive mechanism, which makes it more robust against the “unknown” nature of faulty signals. The adaptation rule is able to find the unknown bounds of faulty signals (which externally impact control feedback) and incorporate them into the control by the sliding-mode-based faulty signal rectifier to form a faulty-signal-tolerant methodology. Thorough theoretical analyses, including stability assessment using the

Lyapunov criterion, are provided in order to design the proposed controller. Comprehensive simulations and experimental results (associated with a GC-VSI) show the effectiveness and reliability of the faulty-signal-tolerant controller, which is proposed in this research.

**Index Terms**—Cyber-physical systems (CPSs), cyber threats, faulty-signal-tolerant controls, grid-connected voltage-source inverter (GC-VSI), modernized microgrid (MMG), multi-infeed ac/dc (MIACDC) power systems, voltage-source inverter (VSI).

## I. INTRODUCTION

THE ENERGY sector has been significantly progressing and moving toward simultaneously integrating power networks and battery energy storage systems embedded in ac/dc power networks—which are also known as multi-infeed ac/dc (MIACDC) power systems in smart grids [1]–[3]. Power systems based on MIACDC architecture can be used in both electric power transmission, e.g., high-voltage direct current systems, and electric power distribution, e.g., active power distribution systems and microgrids (see [1]–[8] and references therein). Once traditional hybrid ac/dc microgrids are highly employed in serving modernized smart grids, they need to have advanced controls. Those microgrids have been named modernized microgrids (MMGs) in this research as they are equipped with innovative controls and sophisticated communications. In smart grids, the MMG concept adds many benefits to the operation, control, and demand supply within commercial power systems. Indeed, having highly novel, sophisticated controls and communications makes traditional hybrid ac/dc microgrids suitable for modernized smart grids. They are the grids with a lot of functionalities and rehabilitating capabilities. MMGs enable the power industry to implement more revolutionary controls (with/without advanced communications) to dramatically improve the reliability, efficiency, operations, dynamics, and power quality (see [6], [9], and references therein).

In smart grids, the modernized MIACDC concept brings many benefits to the operation, control, and demand supply within the commercial power systems. MIACDC-based MMGs will be beneficial to a new trend in power systems’ architecture, which is regarded as a fully integrated power and energy system. The

Manuscript received June 29, 2020; revised October 1, 2020; accepted November 18, 2020. Date of publication December 8, 2020; date of current version March 5, 2021. The work of Masoud Davari was supported by the U.S. National Science Foundation (NSF) under Grants 1808279 and 1902787 awarded by the Core Program of Energy, Power, Control, and Networks (EPCN) in the Division of Electrical, Communications, and Cyber Systems (ECCS). This work was supported in part by SEMIKRON Company, in part by the Verivolt Company, and in part by the dSPACE GmbH Company for Georgia Southern University. Recommended for publication by Associate Editor M. Liserre. (Corresponding author: Masoud Davari.)

Masoud Davari is with the Department of Electrical and Computer Engineering, Allen E. Paulson College of Engineering and Computing, Georgia Southern University (Statesboro Campus), Statesboro, GA 30460 USA (e-mail: davari@ualberta.ca).

Mohammad Pourmahmood Aghababa is with the Department of Electrical and Computer Engineering in the Faculty of Engineering, University of Windsor, Windsor, ON N9B 3P4, Canada, and also with the Electrical Engineering Department, Urmia University of Technology, Urmia 5756151818, Iran (e-mail: m.p.aghababa@gmail.com).

Frede Blaabjerg is with the Department of Energy Technology, Aalborg University, 9220 Aalborg, Denmark (e-mail: fbl@et.aau.dk).

Mehrdad Saif is with the Department of Electrical and Computer Engineering in the Faculty of Engineering, University of Windsor, Windsor, ON N9B 3P4, Canada (e-mail: msaif@uwindsor.ca).

Color versions of one or more figures in this article are available at <https://doi.org/10.1109/TPEL.2020.3042796>.

Digital Object Identifier 10.1109/TPEL.2020.3042796

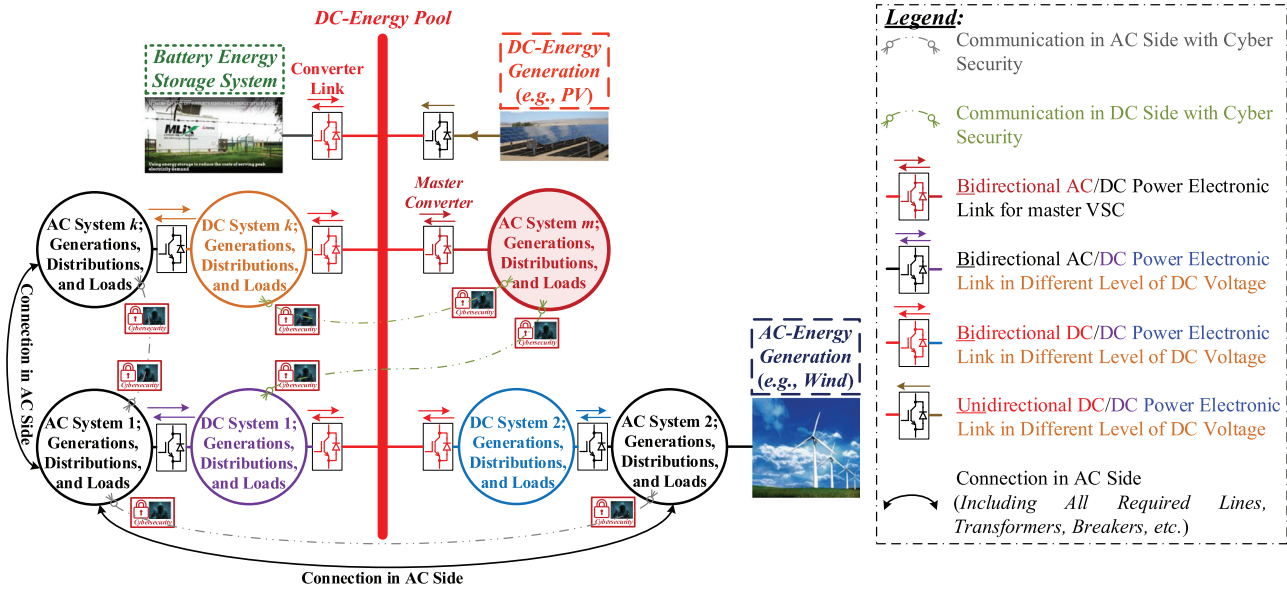


Fig. 1. Notional structure of an MMG based on MIACDC architecture of the fully integrated power and energy system.

“FIPES” abbreviation stands for the “fully integrated power and energy system” phrase if needed in the figures shown in this article wheresoever applicable.

This new trend can surely incorporate battery systems into traditional power systems. An MIACDC-based MMG has a structure similar to what is employed in terrestrial microgrids, but it highly integrates electric power in both “ac” and “dc” networks. MMGs require special considerations in the analysis and studies because their MIACDC power systems significantly utilize a lot of voltage-source-converter-based entities—among which voltage-source inverters (VSIs) have become the vital entities. VSIs will bring more flexibility and add extra capabilities to the MMGs’ operations, e.g., augmented energy management, energy arbitrage in the electricity market, improved power quality, and enhanced dynamics using resilient controls. The MMGs’ fully integrated power and energy systems, as illustrated in Fig. 1, deploy active-/reactive-power-controlled (PQ-controlled), grid-connected VSI in their structure. A PQ-controlled, grid-connected VSI is hereinafter called a GC-VSI to reveal and emphasize the VSI’s mode of operation in this article.

In an architecture like MMG’s fully integrated power and energy system, the use of cyber-physical systems (CPSs) is inevitable. Researchers have proposed different algorithms to be utilized in power systems’ CPSs. For example, the authors in [10] have discussed the standard power systems’ CPS’s infrastructure. The authors have pointed out the importance of cyber infrastructure’s security—along with preventing, mitigating, and tolerating cyber attacks in power application security. It considers all parts’ security in generation units, the issues related to different levels of controls, their evaluation, and risk assessment methodology.

Additionally, the authors in [11] have proposed a cyber-physical multisource energy system applied to electric vehicles. It is based on the genetic algorithm. In that design, two parts exist; the first part shows a multipower supply system

unit containing three energy sources. In contrast, the second part demonstrates an energy management unit to have the optimal control for each source.

Furthermore, CPSs’ algorithms are nowadays progressing. In this regard, researchers have proposed novel CPSs’ algorithms [12]–[18]. The author of [12] has thoroughly investigated fundamental machine learning algorithms in supervised/unsupervised manners and examined new computing architecture for developing the next generation of CPSs for smart grids. A method based on the identification of hybrid dynamical systems for automating the mechanistic modeling of hybrid dynamical systems from observed data has been investigated in [13]. Authors in [14] have proposed a density-based data stream clustering algorithm, built on the multiple species flocking model for monitoring the big data generated from numerous applications. Solution operator discretization methods with linear multistep and implicit Runge–Kutta have been introduced for efficient eigenanalysis of large delayed CPS-based power systems in [15]. Authors in [16] have proposed a cross-adaptive gray wolf optimization algorithm enhanced by adaptive position adjustment tactic. Therein, in order to optimize the prediction model, a cross-optimal solution strategy has been consequently developed. A method based on the pseudospectral discretization of the delayed cyber-physical power system’s solution operator is presented for eigenanalysis in critical electromechanical oscillation modes; they have damping ratios less than a specified threshold described in [17]. Finally, the authors in [18] have carried out a comprehensive assessment of vulnerabilities to cyber threats in Internet-of-Things-based critical infrastructures from the stand-point of applications, networking, operating systems, software, firmware, and hardware.

On the one hand, the recently proposed CPSs’ algorithms can detect more cyber-related issues, and so on [12]–[18], but on the other hand, the hackers’ techniques are getting sophisticated more and more. It means that making any layers/levels—even devices’ primary controls—tolerable

against cyberattack-related issues can help create more reliable, secure, and resilient CPS-based systems. This article has deepened the GC-VSI's primary controls and proposed a faulty signal (hereinafter FS) rectifier in them, which is able to rectify FSs effectively—via an approach that does “not” endanger the closed-loop system's stability. From the standpoint of controls, it is a challenging task because GC-VSIs' controls are the fastest controls with the time constants from 0.5 to 5.0 ms or so—and hence the most inner loops in the controls—in the automation of CPS-based power systems.

Indeed, although the research in this article has considered GC-VSI in CPSs, it has not studied and proposed any new CPS algorithms. Instead, it has been assumed that regular power systems' CPS is being used, e.g., Fig. 1 detailed in [10]. Then, if any FSs are able to reach and catch the GC-VSI's primary control—via a firmware update through CPS, and so forth—the control system is still able to rectify those signals in a way that the “*rigorous*” stability of the device's closed-loop dynamics is preserved.

Indeed, accurate information on the signals (e.g., currents and voltages) is imperative for the controller's successful operation in a healthy and normal situation. It is critical because those signals are used by the primary controller after being converted to the well-known *dq*-frame. Any error in signals (references, feedback, and so on)—which are caused by changes through network—will lead to the generation of erroneous control signals (and hence incorrect modulation indices and switching signals). As a consequence, the related distributed energy resource (DER) fails to operate efficiently.

As elaborated in the articles above (see [10]–[16], and [18]), device controls (e.g., in the generation unit discussed in [10]) are still vulnerable to malware that is potentially able to enter the substation's local area network (also known as LAN) via other entry points such as universal serial bus (commonly known as USB) keys, and more. Other researchers have also pointed out this important matter in CPS-based power systems [18]–[22]. For example, researchers have studied resilient networked ac microgrids [19]. Therefore, no matter how much power systems' CPSs' algorithms are substantial and complicated, there is always a possible way that devices get impacted. In MMGs' CPS-based fully integrated power and energy systems, many automation algorithms have been used in order to ease MMGs' operations. In order to facilitate the automation and operation of GC-VSIs, a lot of control algorithms and signals are being updated and sent through networks and cyber infrastructures. Also, a lot of information is exchanged to increase the flexibility and functionality of the automation process. Therefore, all layers involved in the automation process are susceptible to FSs; undoubtedly, some are easily attacked by cyber threats, while others are harder targeted [18]–[26].

Many layers of security are designed to prevent attacks on hardware firmware, sensors, and so forth, and there exist a lot of algorithms banning them. There are various vulnerabilities associated with each layer, and an attack on any is always possible (it is just a matter of being easier or harder) [27]–[29]. That is why research studies and technical R&D reports have recommended that cyber threats nowadays necessitate engineers

designing and building systems that are able to tolerate FSs from the beginning. As a result, those FSs should be integrated into the system's engineering process [30]–[35]. As a result, there is always a continuous need for proposing controls that are able to “tolerate” FSs on different levels. They are called “faulty-signal-tolerant” controls hereinafter.

To the best of authors' knowledge, there are not faulty-signal-tolerant controls rigorously designed for the primary controls of GC-VSIs, e.g., smart inverters; for the latest research and studies discussing this matter, the reader is referred to [23]–[25] and references therein. This article has researched such a GC-VSI's control in a cyber-physical system of MIACDC-based MMGs. It has investigated this requirement and proposed a simple, yet powerful approach for such a challenging application in the primary control of GC VSIs. The proposed methodology is to make the primary controls robust against FSs, which are not detectable by all means, and impact signals in the *dq*-frame which is one of the well-known frames in which the GC-VSIs are controlled.

This article's fundamental contributions are as follows.

- 1) It enhances the primary output feedback control of GC-VSIs and makes it more reliable by a “signal rectifier” called a faulty signal rectifier. In this article, that control gets augmented and robust against nondetectable faulty signals (or almost nondetectable ones). These are hard to be identified or may not be rejected by security levels.
- 2) It incorporates nondetectable FSs into the state-space representation and proposes a faulty-signal-dependent, dynamic model of GC-VSI, which integrates nondetectable FSs. In this regard, the nondetectable FSs, which affect the primary control, are considered and modeled. In fact, malicious FSs that corrupt or manipulate the flow of data/information, also known as data integrity attack, are modeled and expressed by signals with the subscript of “FS” (stands for the “faulty signal”).
- 3) In this article, while looking at malicious FS as unknown signals, a methodology to reconstruct the GC-VSI's signals externally manipulated by a data integrity issue is proposed. This article develops a strategy that “rectifies” corrupted feedback signals using a nonlinear approach based on a “sliding-mode-based” rectifier with an inherent robustness property. This methodology leads to additional improvements in the reliability of control systems in the primary control layers of GC-VSIs employed in cyber-physical systems for MIACDC-based MMGs. This article names the proposed approach “sliding-mode-based FS rectifier,” which is developed for GC-VSIs. Here, just as an example, the GC-VSI based on the *LCL* ac-side filter, which is industrially accepted and commonly employed in the industry, is used.
- 4) The proposed sliding-mode-based rectifier has an “adaptive” mechanism that is able to take into account the “unknown” bounds of the signals' norms. This way, the rectifier is independent of the specific values associated with the norms of signals and considers them unknown. This consideration is required because the bound of signals externally impacted by FSs is unknown beforehand.

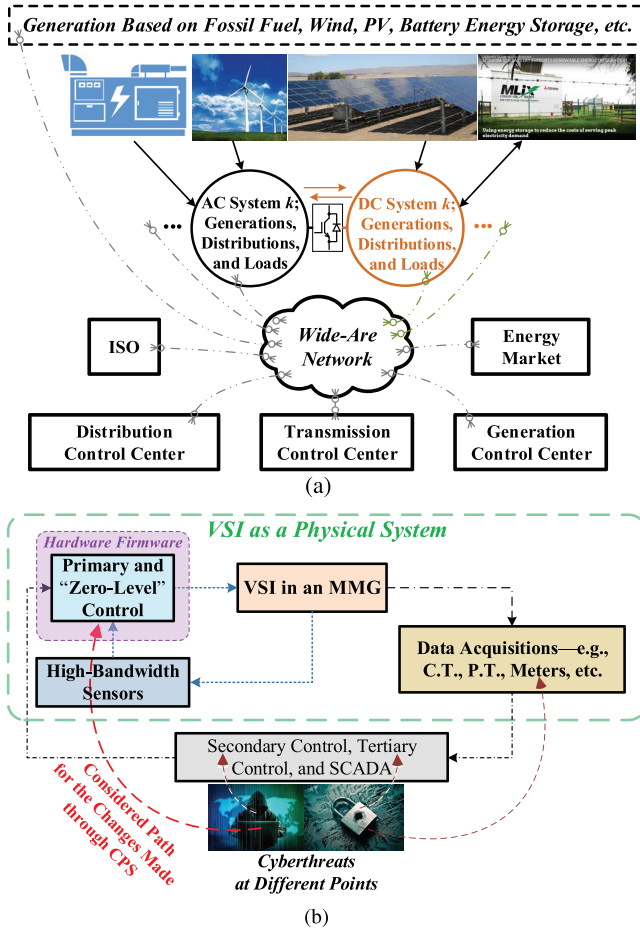


Fig. 2. GC-VSI in the MMGs' CPS-based fully integrated power and energy system. (a) CPS's infrastructure [10]; and (b) considered FSs impacting the primary and zero-level control of a VSI in a cyber-physical system.

The remainder of this article is as follows. Section II mathematically models the system under study, i.e., *LCL*-VSI, in the state-space representation. Section III details the sliding-mode-based FS rectifier. Section IV demonstrates the simulations and experimental results. Finally, Section V concludes the article.

## II. SYSTEM UNDER STUDY

Considering Fig. 3, the describing state-space representation of (1)–(4) models the dynamics of a GC-VSI equipped with an *LCL*-filter. In (1), the state vector of  $\mathbf{x}$  is defined as  $[i_{1d} \ i_{1q} \ i_{2d} \ i_{2q} \ v_{cf_d} \ v_{cf_q}]^T$ , the input vector of  $\mathbf{u}$  is described as  $[m_d \ m_q]^T$ , the output vector of  $\mathbf{y}$  is expressed as  $[i_{2d} \ i_{2q} \ v_{cf_d} \ v_{cf_q}]^T$ , and the disturbance vector of  $\mathbf{d}$  is defined as  $[v_{PCC_d} \ v_{PCC_q}]^T$ . In the vectors stated earlier, based on Fig. 3,  $i_{1d}$  and  $i_{1q}$  are the *dq*-components of the space phasor of  $\vec{i}_1$  representing  $i_{1a}$ ,  $i_{1b}$ , and  $i_{1c}$ ;  $i_{2d}$  and  $i_{2q}$  are the *dq*-components of the space phasor of  $\vec{i}_2$  representing  $i_{2a}$ ,  $i_{2b}$ , and  $i_{2c}$ ;  $v_{cf_d}$  and  $v_{cf_q}$  are the *dq*-components of the space phasor of  $\vec{v}_{cf}$  representing  $v_{cf_a}$ ,  $v_{cf_b}$ , and  $v_{cf_c}$ ;  $v_{PCC_d}$  and  $v_{PCC_q}$  are

the *dq*-components of the space-phasor of  $\vec{v}_{PCC}$  representing point of common coupling (PCC) voltages of  $v_{PCC_a}$ ,  $v_{PCC_b}$ , and  $v_{PCC_c}$ ; and  $m_d$  and  $m_q$  are the modulation indices of the switching scheme based on the pulse width modulation (PWM) methodology in the *dq*-frame

$$\begin{cases} \dot{\mathbf{x}} = \mathbf{A}\mathbf{x} + \mathbf{B}_1\mathbf{u} + \mathbf{B}_2\mathbf{d} \\ \mathbf{y} = \mathbf{C}\mathbf{x} \end{cases} \quad (1)$$

where the “over dot” denotes the time derivative

$$\mathbf{A} = \begin{bmatrix} -\frac{R_{t1}}{L_{f1}} & \omega & \frac{R_f}{L_{f1}} & 0 & -\frac{1}{L_{f1}} & 0 \\ -\omega & -\frac{R_{t1}}{L_{f1}} & 0 & \frac{R_f}{L_{f1}} & 0 & -\frac{1}{L_{f1}} \\ \frac{R_f}{L_{f2}} & 0 & -\frac{R_{t2}}{L_{f2}} & \omega & \frac{1}{L_{f2}} & 0 \\ 0 & \frac{R_f}{L_{f1}} & -\omega & -\frac{R_{t2}}{L_{f2}} & 0 & \frac{1}{L_{f2}} \\ \frac{1}{C_f} & 0 & -\frac{1}{C_f} & 0 & 0 & \omega \\ 0 & \frac{1}{C_f} & 0 & -\frac{1}{C_f} & -\omega & 0 \end{bmatrix} \quad (2)$$

$$\mathbf{B}_1 = \frac{v_{dc}}{2} \begin{bmatrix} \frac{1}{L_{f1}} & 0 \\ 0 & \frac{1}{L_{f1}} \\ 0 & 0 \\ 0 & 0 \\ 0 & 0 \\ 0 & 0 \end{bmatrix}, \quad \mathbf{B}_2 = \begin{bmatrix} 0 & 0 \\ 0 & 0 \\ -\frac{1}{L_{f2}} & 0 \\ 0 & -\frac{1}{L_{f2}} \\ 0 & 0 \\ 0 & 0 \end{bmatrix} \quad \text{and} \quad (3)$$

$$\mathbf{C} = \begin{bmatrix} 0 & 0 & 1 & 0 & 0 & 0 \\ 0 & 0 & 0 & 1 & 0 & 0 \\ 0 & 0 & 0 & 0 & 1 & 0 \\ 0 & 0 & 0 & 0 & 0 & 1 \end{bmatrix}. \quad (4)$$

In (1)–(4),  $R_{t1} \triangleq R_{f1} + R_f$  and  $R_{t2} \triangleq R_{f2} + R_f$ ;  $L_{f1}/R_{f1}$  are the *LCL*-filter's converter-side inductance/resistance;  $L_{f2}/R_{f2}$  is *LCL*-filter's ac-grid-side inductance/resistance; and  $C_f$  is the *LCL*-filter's shunt capacitance. All of the variable mentioned above have been shown in Fig. 3.

Equation (1) describes the “faulty-signal-free” dynamics of the GC-VSI in Fig. 3. If FSs appear in the output vector of  $\mathbf{y}$  in (1)—without loss of generality—it becomes as follows:

$$\begin{cases} \dot{\mathbf{x}} = \mathbf{A}\mathbf{x} + \mathbf{B}_1\mathbf{u} + \mathbf{B}_2\mathbf{d} \\ \mathbf{y} = \mathbf{C}\mathbf{x} + \mathbf{E}\mathbf{f}_{FS} \end{cases} \quad (5)$$

where  $\mathbf{A}$ ,  $\mathbf{B}_1$ ,  $\mathbf{B}_2$ , and  $\mathbf{C}$  are defined through (2)–(4), and the vector of  $\mathbf{f}_{FS}$  constitutes FSs targeting the output vector of  $\mathbf{y}$  in the primary control of the given GC-VSI. Moreover,  $\mathbf{E}$  is the FSs' impacts' distribution matrix, and  $\mathbf{f}_{FS}$  is the vector incorporating errors caused by an FS.

It should be noted that any falsifying FSs added to the measurements in order to externally manipulate and corrupt them result in the generation of erroneous control signals (and incorrect modulation indices and switching signals), thus causing DER to operate incorrectly. In this regard, equation (5) has developed a “faulty-signal-dependent” model for GC-VSIs with an *LCL*-filter by considering an additional signal associated with errors added to the output and by incorporating it within the

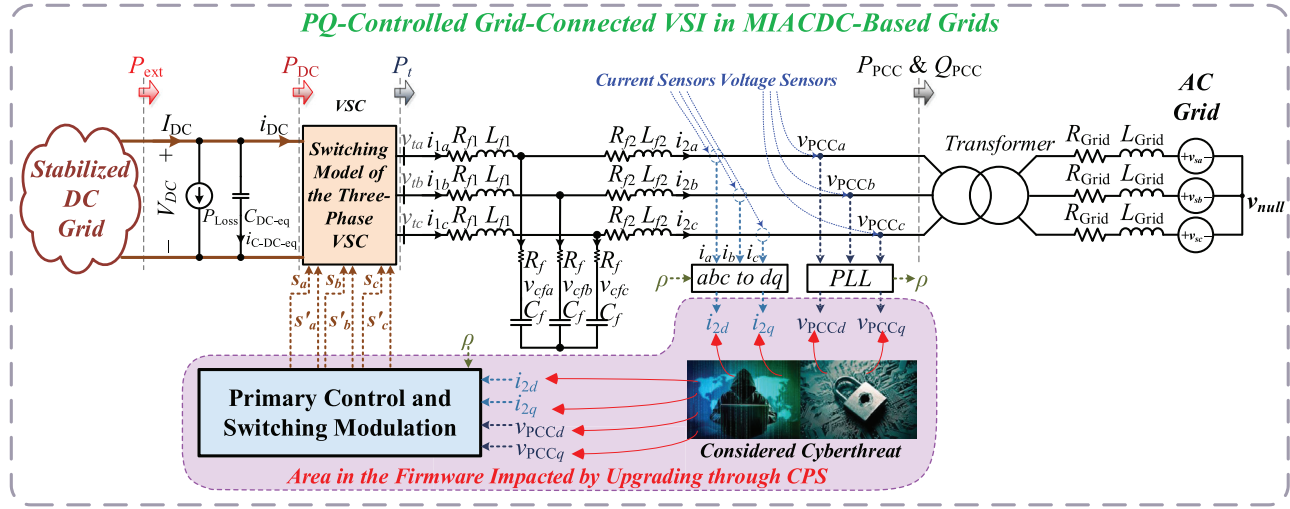


Fig. 3. Detailed block diagram of the *LCL*-based GC-VSIs used in the MIADC-based MMGs showing the considered FSs.

faulty-signal-tolerant control design process as follows. Then, a faulty-signal-tolerant control strategy can be proposed. It modifies the control approach presented above to ensure resiliency against FSs, using a sliding-mode-based faulty-signal-rectifying approach. In order to tackle this problem, the next section details the proposed method to construct the error in the measurements and use the reconstructed signals in a faulty-signal-tolerant control scheme.

According to (5), since it is required to derive a faulty-signal-dependent model for the system in our problem formulation, it means that a time-varying system is being involved. As a result, it is very challenging to find Lyapunov functions with a negative definite derivative to prove the asymptotic stability of such a system (see [36]). It is well known that in case of dealing with time-invariant systems—if the time derivative of the Lyapunov function is negative semidefinite—then it is possible to conclude the asymptotic behaviors by benefiting from invariant-set theorems [36].

Notwithstanding, such flexibility is not available to time-varying systems. Barbalat's Lemma is key to this problem historically. In order to be able to benefit from Barbalat's Lemma, the FSs impacting the output should be bounded. As a consequence, Remark 1 below has revealed this requirement. It is worthy of mention that considering Remark 1 does not impose any restrictions on this research's scope because it is assumed that the CPSs have not detected FSs. Therefore, there are many layers that have already seen detectable signals as those are not able to reach the devices' controls.

*Remark 1:* In (5), it is assumed that  $\|\mathbf{E}\mathbf{f}_{\text{FS}}\|_2$  and  $\|\mathbf{E}\dot{\mathbf{f}}_{\text{FS}}\|_2$  are bounded—in which  $\|\cdot\|_2$  calculates the 2-norm of a vector. This assumption does not impact the generality of the considered problem formulation since this article looks at as “nondetectable” as possible FSs.

Since the “current-controlled, PWM-based” structure is employed (which is very well known and attractive because of its salient features), a control system ensures fast reference tracking, i.e.,  $i_{2d} \rightarrow i_{2d\text{-ref}}$  and  $i_{2q} \rightarrow i_{2q\text{-ref}}$  then  $P_{\text{PCC}} \rightarrow P_{\text{PCC-ref}}$  and

$Q_{\text{PCC}} \rightarrow Q_{\text{PCC-ref}}$ .  $i_{2d\text{-ref}}$  is the reference signal of  $i_{2d}$ ,  $i_{2q\text{-ref}}$  is the reference signal of  $i_{2q}$ ,  $P_{\text{PCC-ref}}$  is reference signal of the active power injected to PCC, and  $Q_{\text{PCC-ref}}$  is reference signal of the reactive power injected to PCC. Based on the operation of a GC-VSI using current-controlled, PWM-based methodology, which benefits from a decoupled active/reactive power control through the phase-locked loop (PLL), the reference signals of  $i_{2d\text{-ref}}$  and  $i_{2q\text{-ref}}$  can be expressed as

$$\begin{cases} i_{2d\text{-ref}} = \frac{2P_{\text{PCC-ref}}}{3v_{\text{PCC}d}} \\ i_{2q\text{-ref}} = \frac{-2Q_{\text{PCC-ref}}}{3v_{\text{PCC}d}}. \end{cases} \quad (6)$$

### III. SLIDING-MODE-BASED FS RECTIFIER

This section details the proposed FS rectifier, which is based on sliding mode. In this regard, an “adaptive” FS rectifier for the system of (5) is synthesized. Now, in order to rectify the FSs, the a vector containing sliding surfaces around which the sliding regiments will be induced is required to be defined. The vector of sliding variable  $\mathbf{s} = [s_1 s_2 s_3 s_4]^T \in \mathbb{R}^4$  is first introduced. For doing so, an auxiliary vector variable of  $\mathbf{z} = [z_1 z_2 z_3 z_4]^T \in \mathbb{R}^4$  is also required to be defined as follows:

$$\begin{cases} \mathbf{s} \triangleq \mathbf{z} - \mathbf{y}, \\ \mathbf{z} \triangleq \mathbf{C}\mathbf{x} - \int_0^t (k_r + \hat{\alpha}) \text{sign}(\mathbf{s}(\tau)) d\tau \end{cases} \quad (7)$$

where  $k_r > 0$  is a constant, and  $\hat{\alpha}$  is a time-dependent function, whose dynamics are expressed below.

Now, using  $\mathbf{y}$  defined in (5) and (7)

$$\begin{aligned} \mathbf{s} &= \mathbf{z} - \mathbf{C}\mathbf{x} - \mathbf{E}\mathbf{f}_{\text{FS}} \\ \Rightarrow \mathbf{E}\mathbf{f}_{\text{FS}} &= \mathbf{z} - \mathbf{C}\mathbf{x} - \mathbf{s}. \end{aligned} \quad (8)$$

Therefore,  $\dot{\mathbf{s}} = \dot{\mathbf{z}} - \dot{\mathbf{y}} \Rightarrow \dot{\mathbf{s}} = \dot{\mathbf{z}} - \mathbf{C}\dot{\mathbf{x}} - \mathbf{E}\dot{\mathbf{f}}_{\text{FS}}$

$$\Rightarrow \mathbf{E}\dot{\mathbf{f}}_{\text{FS}} = \dot{\mathbf{z}} - \mathbf{C}\dot{\mathbf{x}} - \dot{\mathbf{s}}.$$

Then, supposing  $\|\mathbf{E}\dot{\mathbf{f}}_{\text{FS}}\|_2 \leq \alpha_1$  and  $\|\mathbf{C}\dot{\mathbf{x}}\|_2 \leq \beta\|\mathbf{x}\|_2 + \alpha_2$ , where  $\alpha_1 > 0$ ,  $\alpha_2 > 0$ , and  $\beta > 0$  are unknown constants—in which it is assumed that there is an  $\alpha$ , so that  $\alpha_1 + \alpha_2 \leq \alpha$ . Next, the adaptive dynamics are defined as

$$\begin{cases} \dot{\mathbf{z}} = -(\hat{\beta}\|\mathbf{x}\|_2 + \hat{\alpha} + k_r)\text{sign}(\mathbf{s}) \\ \dot{\hat{\alpha}} = \eta\|\mathbf{s}\|_2 \\ \dot{\hat{\beta}} = \zeta\|\mathbf{s}\|_2\|\mathbf{x}\|_2 \end{cases} \quad (9)$$

where  $\mathbf{z}(0) = \mathbf{0}$ ,  $\hat{\alpha}(0) = \hat{\alpha}_0 > 0$ , and  $\hat{\beta}(0) = \hat{\beta}_0 > 0$  (i.e.,  $\hat{\alpha}_0$  and  $\hat{\beta}_0$  are the initial value of the adaptive dynamics),  $\eta > 0$  is a constant, and  $\text{sign}(\mathbf{s}) \triangleq [\text{sign}(s_1)\text{sign}(s_2)\text{sign}(s_3)\text{sign}(s_4)]^T$ . It is noteworthy that (9) is an adaptive dynamic system, which is able to deal with and tackle the limited upper bound of FSs, which are assumed unknown beforehand. It is a rational assumption as the upper bound of FSs—which can be created by “any” sources—are unknown.

*Remark 2:* Considering  $\dot{\hat{\alpha}}$  and  $\dot{\hat{\beta}}$  [described in (9)], it is obvious that  $\hat{\alpha}(t) > 0$  and  $\hat{\beta}(t) > 0$ .

This article proves that the adaptive dynamics of (9) are stable, as shown in the following theorem.

*Theorem 1 (Stability of the FS rectifier):* Consider the uncertain system of (5) along with the auxiliary variables of  $\mathbf{s}$  and  $\mathbf{z}$  defined above. The origin is the stable equilibrium point of the adaptive dynamical FS “rectifier” of (9).

*Proof:* The Lyapunov function of  $V_{\text{rect}}(t)$  is defined as

$$V_{\text{rect}}(t) = \frac{1}{2}\|\mathbf{s}\|_2^2 + \frac{1}{2\eta}\tilde{\alpha}^2 + \frac{1}{2\zeta}\tilde{\beta}^2 \quad (10)$$

where  $\tilde{\alpha} \triangleq \alpha - \hat{\alpha}$  and  $\tilde{\beta} \triangleq \beta - \hat{\beta}$ .

From (10)

$$\dot{V}_{\text{rect}}(t) = \mathbf{s}^T \dot{\mathbf{s}} - \frac{\dot{\hat{\alpha}}}{\eta}(\alpha - \hat{\alpha}) - \frac{\dot{\hat{\beta}}}{\zeta}(\beta - \hat{\beta}). \quad (11)$$

From (8) and (9), (11) is expressed as

$$\begin{aligned} \dot{V}_{\text{rect}}(t) &= \mathbf{s}^T(\dot{\mathbf{z}} - \mathbf{C}\dot{\mathbf{x}} - \mathbf{E}\dot{\mathbf{f}}_{\text{FS}}) - \|\mathbf{s}\|_2(\alpha - \hat{\alpha}) \\ &\quad - \|\mathbf{s}\|_2\|\mathbf{x}\|_2(\beta - \hat{\beta}). \end{aligned} \quad (12)$$

As a result, (9) and (12) conclude that

$$\begin{aligned} \dot{V}_{\text{rect}}(t) &\leq \mathbf{s}^T\dot{\mathbf{z}} + \|\mathbf{s}\|_2(\|\mathbf{C}\dot{\mathbf{x}}\| + \|\mathbf{E}\dot{\mathbf{f}}_{\text{FS}}\|_2) \\ &\quad - \|\mathbf{s}\|_2(\alpha - \hat{\alpha}) - \|\mathbf{s}\|_2\|\mathbf{x}\|_2(\beta - \hat{\beta}). \end{aligned} \quad (13)$$

Using (13),  $\dot{V}_{\text{rect}}(t)$  is expressed as

$$\begin{aligned} \dot{V}_{\text{rect}}(t) &\leq -\mathbf{s}^T(\hat{\beta}\|\mathbf{x}\|_2 + \hat{\alpha} + k_r)\text{sign}(\mathbf{s}) \\ &\quad + \|\mathbf{s}\|_2(\beta\|\mathbf{x}\|_2 + \alpha_2 + \alpha_1) - \|\mathbf{s}\|_2(\alpha - \hat{\alpha}) \\ &\quad - \|\mathbf{s}\|_2\|\mathbf{x}\|_2(\beta - \hat{\beta}). \end{aligned} \quad (14)$$

From (14) and by using  $\mathbf{s}^T\text{sign}(\mathbf{s}) = \|\mathbf{s}\|_1$ , the upper bound of  $\dot{V}_{\text{rect}}(t)$  is described as

$$\begin{aligned} \dot{V}_{\text{rect}}(t) &\leq -\mathbf{s}^T(\hat{\beta}\|\mathbf{x}\|_2 + \hat{\alpha} + k_r)\text{sign}(\mathbf{s}) \\ &\quad + \hat{\alpha}\|\mathbf{s}\|_2 + \hat{\beta}\|\mathbf{s}\|_2\|\mathbf{x}\|_2 \\ \Rightarrow \dot{V}_{\text{rect}}(t) &\leq -\hat{\beta}\|\mathbf{x}\|_2\|\mathbf{s}\|_1 - \hat{\alpha}\|\mathbf{s}\|_1 - k_r\|\mathbf{s}\|_1 + \hat{\alpha}\|\mathbf{s}\|_2 \\ &\quad + \hat{\beta}\|\mathbf{s}\|_2\|\mathbf{x}\|_2 \\ \Rightarrow \dot{V}_{\text{rect}}(t) &\leq \underbrace{\hat{\alpha}(\|\mathbf{s}\|_2 - \|\mathbf{s}\|_1)}_{\text{A Negative Term}} + \underbrace{\hat{\beta}(\|\mathbf{s}\|_2\|\mathbf{x}\|_2 - \|\mathbf{s}\|_1\|\mathbf{x}\|_2)}_{\text{A Negative Term}} \\ &\quad - k_r\|\mathbf{s}\|_1 \\ \Rightarrow \dot{V}_{\text{rect}}(t) &< -k_r\|\mathbf{s}\|_1 < 0. \end{aligned} \quad (15)$$

It is noteworthy that (15) has been concluded considering  $\|\mathbf{s}\|_2 \leq \|\mathbf{s}\|_1$  (hence  $\|\mathbf{s}\|_2\|\mathbf{x}\|_2 \leq \|\mathbf{s}\|_1\|\mathbf{x}\|_2$ ),  $\hat{\alpha} > 0$ , and  $\hat{\beta} > 0$ . Therefore, the proof is completed. ■

*Remark 3:* Because of the existing discontinuous “sign” function in Theorem 1—e.g., in (9) and anywhere else employed in this article’s sliding-mode-based algorithms hereinafter—it is well known that the conventional sliding mode controllers may show the chattering phenomenon appearing on the outputs. An alternative to reduce the chattering effects is commonly known as the boundary layer method, which has been adopted in this article. Therefore, a saturation function approximates the sign function. This article has utilized the continuous, smooth, hyperbolic tangent function [i.e.,  $\tanh(\epsilon_{\text{BL}}\mathbf{s})$ ] to replace the sign function with a smooth one wherever needed. In  $\tanh(\epsilon_{\text{BL}}\mathbf{s})$ , the positive  $\epsilon_{\text{BL}}$  converges the tanh function to the sign one—by changing the slope at the point of discontinuity—the lower the value of  $\epsilon_{\text{BL}}$  is, the less the chattering effect arises. This alternative methodology eliminates the discontinuity of the control signal, thereby avoiding the chattering phenomenon and its issues [37]–[39]. It is worthy of mention that detailing, discussing, addressing, and dealing with different chattering issues of sliding-mode-based controls’ theories are not directly within this article’s scope (see [38], [39]).

*Corollary 1 (Estimation of the FS):* The vector of  $\mathbf{E}\hat{\mathbf{f}}_{\text{FS}}$  is defined as  $\mathbf{E}\hat{\mathbf{f}}_{\text{FS}} \triangleq \mathbf{z} + \mathbf{C}\mathbf{x}$ , where  $\hat{\mathbf{f}}_{\text{FS}}$  is an estimation of the FS vector of  $\mathbf{f}_{\text{FS}}$ . By defining  $\tilde{\mathbf{f}}_{\text{FS}}$  as the FS error vector, one can prove that  $\tilde{\mathbf{f}}_{\text{FS}}$  reaches  $\mathbf{0}$  as  $t \rightarrow \infty$  (i.e.,  $\tilde{\mathbf{f}}_{\text{FS}} \rightarrow \mathbf{0}$  as  $t \rightarrow \infty$ ), or equivalently  $\hat{\mathbf{f}}_{\text{FS}}$  reaches  $\mathbf{f}_{\text{FS}}$  (i.e.,  $\hat{\mathbf{f}}_{\text{FS}} \rightarrow \mathbf{f}_{\text{FS}}$ ) as  $t \rightarrow \infty$ .

*Proof:* By defining  $\mathbf{f}_{\text{FS}}$  as the FS error vector, (16) is obtained as

$$\tilde{\mathbf{f}}_{\text{FS}} = \hat{\mathbf{f}}_{\text{FS}} - \mathbf{f}_{\text{FS}}, \Rightarrow \dot{\tilde{\mathbf{f}}}_{\text{FS}} = \dot{\hat{\mathbf{f}}}_{\text{FS}} - \dot{\mathbf{f}}_{\text{FS}}. \quad (16)$$

$\dot{\tilde{\mathbf{f}}}_{\text{FS}}$ ’s definition in Corollary 1 concludes that  $\dot{\tilde{\mathbf{f}}}_{\text{FS}} = \dot{\mathbf{z}} + \mathbf{C}\dot{\mathbf{x}} - \dot{\mathbf{f}}_{\text{FS}}$ .

Also, from (5),  $\mathbf{E}\dot{\mathbf{f}} = \dot{\mathbf{y}} - \mathbf{C}\dot{\mathbf{x}}$  is obtained. Consequently

$$\dot{\tilde{\mathbf{f}}}_{\text{FS}} = \dot{\mathbf{z}} + \mathbf{C}\dot{\mathbf{x}} - (\dot{\mathbf{y}} - \mathbf{C}\dot{\mathbf{x}}) = \dot{\mathbf{z}} - \dot{\mathbf{y}}. \quad (17)$$

Considering the definition of  $\mathbf{s}$  (i.e.,  $\mathbf{s} \triangleq \mathbf{z} - \mathbf{y}$ ), equation (17) becomes  $\dot{\tilde{\mathbf{f}}}_{\text{FS}} = \dot{\mathbf{z}} - \dot{\mathbf{y}} = \dot{\mathbf{s}}$ .

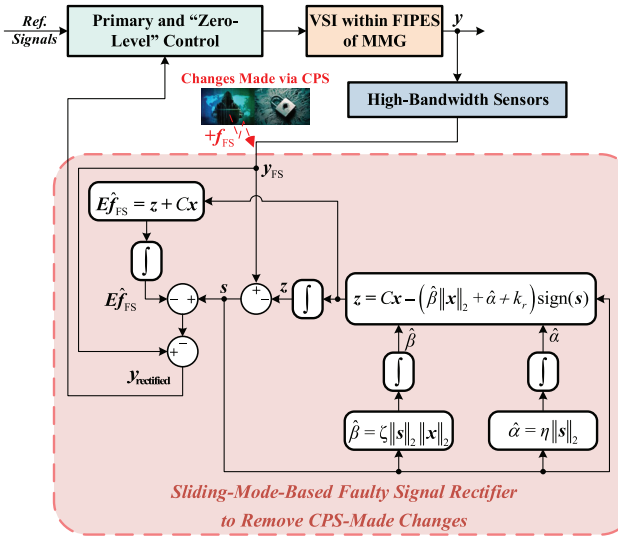


Fig. 4. Proposed faulty-signal-tolerant control for GC-VSIs.

As a consequence, according to Theorem 1, since  $s$  reaches zero (i.e.,  $s \rightarrow 0$ ) as  $t$  goes to infinity (i.e.,  $t \rightarrow \infty$ )—based on Barbalat’s Lemma (see [36])—and since  $\|E\mathbf{f}_{FS}\|_2$  and  $\|\hat{E}\mathbf{f}_{FS}\|_2$  are bounded, one can conclude that  $\hat{\mathbf{f}}_{FS} \rightarrow \mathbf{0}$  as  $t \rightarrow \infty$ . Therefore, as  $t \rightarrow \infty$ ,  $\hat{\mathbf{f}}_{FS} \rightarrow \mathbf{f}_{FS}$ , which completes the proof.

Fig. 4 has shown the detailed control structure of the proposed sliding-mode-based FS rectifier. The microscopic structure of the VSI shown in Fig. 4—including the switching signals of Phase A (i.e.,  $S_a$  for upper leg A and  $S'_a$  for the lower one), Phase B (i.e.,  $S_b$  for upper leg B and  $S'_b$  for the lower one), and Phase C (i.e.,  $S_c$  for upper leg C and  $S'_c$  for the lower one)—has been shown in Fig. 3.

Next, Corollary 2 has demonstrated that one is able to integrate the proposed sliding-mode-based FS rectifier of (9) into any currently stabilizing output feedback controller, which equips the VSI with any desired performance.

*Corollary 2 (FS rectifier embedded in an existing output feedback controller):* Considering the stable sliding-mode-based FS rectifier of the adaptive dynamics of (9) and referring to Fig. 4, the uncertain system of (5) can be controlled by any currently stabilizing output feedback controller for the VSI.

*Proof:* Suppose that  $\mathbf{u} = -\mathbf{K}\mathbf{y} = -\mathbf{K}\mathbf{C}\mathbf{x}$  is a currently working output feedback controller employed in the  $LCL$ -VSI. Then, if  $\mathbf{u} = -\mathbf{K}(\mathbf{y} + \Delta)$  is chosen, in which  $\mathbf{K}$  is the output feedback control gain, then

$$\mathbf{u} = -\mathbf{K}(\mathbf{y} + \Delta) = -\mathbf{K}(\mathbf{C}\mathbf{x} + \mathbf{E}\mathbf{f}_{FS} + \Delta). \quad (18)$$

Provided that  $\Delta = -(\mathbf{E}\hat{\mathbf{f}}_{FS} - s)$ , it is proved that

$$\mathbf{u} = -\mathbf{K}(\mathbf{C}\mathbf{x} + \mathbf{E}\mathbf{f} - (\mathbf{E}\hat{\mathbf{f}}_{FS} - s)). \quad (19)$$

Assuming  $s(0) = \hat{\mathbf{f}}_{FS}(0) = \mathbf{0}$  and considering  $\mathbf{E}\hat{\mathbf{f}}_{FS} = \dot{\mathbf{z}} - \dot{\mathbf{y}} = \dot{s}$ , (19) is simplified as  $\mathbf{E}\hat{\mathbf{f}}_{FS} - s = \mathbf{E}\mathbf{f}_{FS}$ , which inserting it into (19) proves that  $\mathbf{u} = -\mathbf{K}\mathbf{C}\mathbf{x} = -\mathbf{K}\mathbf{y}$ . It is noteworthy

that  $\mathbf{u}$  is the main output feedback controller that has been applied to the system, so it proves Corollary 2. ■

Fig. 4 has shown the block diagram of the faulty-signal-tolerant control for GC-VSIs, including the proposed sliding-mode-based FS rectifier in detail.

For the controller, for example, a two degree-of-freedom (2DoF) structure enhanced by an adaptive design can be used and synthesized here. Regarding the system as a 2DoF system (see [40]), the following equations are able to model the dynamics of the grid-side filter’s currents (in the  $dq$ -frame) using a 2DoF system as required for controlling active power and reactive power [40]

$$\begin{cases} \dot{i}_{2d}(t) = \omega_0(t)i_{2q}(t) - \frac{R_{t2}}{L_{f2}}i_{2d}(t) - \frac{v_{PCCd}(t)}{L_{f2}} + \frac{u_{i_{2d}}(t)}{L_{f2}} \\ \dot{i}_{2q}(t) = -\omega_0(t)i_{2d}(t) - \frac{R_{t2}}{L_{f2}}i_{2q}(t) - \frac{v_{PCCq}(t)}{L_{f2}} + \frac{u_{i_{2q}}(t)}{L_{f2}}. \end{cases} \quad (20)$$

Therefore, considering (20), the dynamics of the tracking errors of  $e_{i_{2d}} \triangleq i_{2d} - i_{2d\text{-ref}}$  and  $e_{i_{2q}} \triangleq i_{2q} - i_{2q\text{-ref}}$  are expressed as follows:

$$\begin{cases} \dot{e}_{i_{2d}}(t) = \omega_0(t)i_{2q}(t) - \frac{R_{t2}}{L_{f2}}i_{2d}(t) - \frac{v_{PCCd}(t)}{L_{f2}} + \frac{u_{i_{2d}}(t)}{L_{f2}} - \dot{i}_{2d\text{-ref}}(t) \\ \dot{e}_{i_{2q}}(t) = -\omega_0(t)i_{2d}(t) - \frac{R_{t2}}{L_{f2}}i_{2q}(t) - \frac{v_{PCCq}(t)}{L_{f2}} + \frac{u_{i_{2q}}(t)}{L_{f2}} - \dot{i}_{2q\text{-ref}}(t). \end{cases} \quad (21)$$

It is assumed that  $i_{2d\text{-ref}}$ ,  $i_{2d}$ ,  $i_{2q\text{-ref}}$ , and  $i_{2q}$  are accessible, and  $i_{2d}$  and  $i_{2q}$  are the outcomes of the proposed rectifier, which is able to properly rectify the FSs’ impacts in a stable fashion. Now, it is possible to consider  $v_{PCCd}$ ,  $v_{PCCq}$ ,  $L_{f2}$ ,  $R_{t2}$ , and  $\omega_0$  are not known but limited. The best initial guesses are their nominal values as well. This way, the changes impacting their values (by grid’s changes or FSs) are considered and updated adaptively. Therefore, for the parameters’ estimations, the following dynamics have been taken into account:

$$\begin{cases} \dot{\hat{L}}_{f2}(t) = -\mathcal{K}_{L_{f2}}(e_{i_{2d}}(t)\dot{i}_{2d\text{-ref}}(t) + e_{i_{2q}}(t)\dot{i}_{2q\text{-ref}}(t)) \\ \dot{\hat{R}}_{t2}(t) = -\mathcal{K}_{R_{t2}}(e_{i_{2d}}(t)i_{2d}(t) + e_{i_{2q}}(t)i_{2q}(t)) \\ \dot{\hat{X}}_{f2}(t) = +\mathcal{K}_{X_{f2}}(e_{i_{2d}}(t)i_{2q}(t) - e_{i_{2q}}(t)i_{2d}(t)) \\ \dot{\hat{V}}_{PCCd}(t) = -\mathcal{K}_{v_{PCCd}}e_{i_{2d}}(t) \\ \dot{\hat{V}}_{PCCq}(t) = -\mathcal{K}_{v_{PCCq}}e_{i_{2q}}(t) \end{cases} \quad (22)$$

in which  $\mathcal{K}_{L_{f2}}$ ,  $\mathcal{K}_{R_{t2}}$ ,  $\mathcal{K}_{X_{f2}}$ ,  $\mathcal{K}_{v_{PCCd}}$ , and  $\mathcal{K}_{v_{PCCq}}$  are all positive values, and the initial values of the functions above are the positive, nominal values of  $L_{f2}$ ,  $R_{t2}$ ,  $X_{f2} \triangleq \omega_0 L_{f2}$  (i.e., the nominal impedance of  $L_{f2}$  at the nominal frequency of  $\omega_0$ ),  $v_{PCCd}$ , and  $v_{PCCq}$ , respectively.

After that, considering (21) and (22), the following input signals are able to stabilize (21) according to *Theorem 2*

$$\begin{cases} u_{i_{2d}} = \hat{R}_{t2}(t)i_{2d} - \hat{X}_{L_{f2}}(t)i_{2q} + \hat{V}_{PCCd}(t) \\ \quad + \hat{L}_{f2}(t)\dot{i}_{2d\text{-ref}} - k_{e_{i_{2d}}}\text{sign}(e_{i_{2d}}(t)) \\ u_{i_{2q}} = \hat{R}_{t2}(t)i_{2q} + \hat{X}_{L_{f2}}(t)i_{2d} + \hat{V}_{PCCq}(t) \\ \quad + \hat{L}_{f2}(t)\dot{i}_{2q\text{-ref}} - k_{e_{i_{2q}}}\text{sign}(e_{i_{2q}}(t)) \end{cases} \quad (23)$$

where  $k_{e_{i_{2d}}}$  and  $k_{e_{i_{2q}}}$  are positive numbers, and  $\hat{X}_{L_{f2}} \triangleq \hat{\omega}\hat{L}_{f2}$ .

**Theorem 2 (Stability of the adaptive controller):** Consider the system of (21) with adaptive dynamics of (22) with the inputs defined in (23). The origin is the stable equilibrium point of the closed-loop system described.

*Proof:* The Lyapunov function of  $V_{\text{contr}}(t)$  is expressed as

$$V_{\text{contr}}(t) = \frac{1}{2} \left( L_{f2} \|e(t)\|_2^2 + \frac{\tilde{L}_{t2}^2(t)}{\mathcal{K}_{L_{f2}}} + \frac{\tilde{R}_{t2}^2(t)}{\mathcal{K}_{R_{t2}}} + \frac{\tilde{X}_{L_{f2}}^2(t)}{\mathcal{K}_{X_{f2}}} \right. \\ \left. + \frac{\tilde{V}_{\text{PCC}_d}^2(t)}{\mathcal{K}_{v_{\text{PCC}_d}}} + \frac{\tilde{V}_{\text{PCC}_q}^2(t)}{\mathcal{K}_{v_{\text{PCC}_q}}} \right) \quad (24)$$

where

$$\begin{cases} e(t) \triangleq [e_{i_{2d}}(t), e_{i_{2q}}(t)]^T \\ \tilde{L}_{f2}(t) \triangleq L_{f2} - \hat{L}_{f2}(t) \\ \tilde{R}_{t2}(t) \triangleq R_{t2} - \hat{R}_{t2}(t) \\ \tilde{X}_{L_{f2}} \triangleq X_{L_{f2}} - \hat{X}_{L_{f2}}(t) \\ \tilde{V}_{\text{PCC}_d}(t) \triangleq v_{\text{PCC}_d} - \hat{V}_{\text{PCC}_d}(t) \\ \tilde{V}_{\text{PCC}_q}(t) \triangleq v_{\text{PCC}_q} - \hat{V}_{\text{PCC}_q}(t). \end{cases} \quad (25)$$

Thus,  $\dot{V}_{\text{contr}}(t)$  is found as

$$\dot{V}_{\text{contr}}(t) = L_{f2} \dot{e}_{i_{2d}}(t) e_{i_{2d}}(t) + L_{f2} \dot{e}_{i_{2q}}(t) e_{i_{2q}}(t) \\ - \frac{\dot{\tilde{L}}_{f2}(t) (L_{f2} - \hat{L}_{f2}(t))}{\mathcal{K}_{L_{f2}}} - \frac{\dot{\tilde{R}}_{t2}(t) (R_{t2} - \hat{R}_{t2}(t))}{\mathcal{K}_{R_{t2}}} \\ - \frac{\dot{\tilde{X}}_{L_{f2}}(t) (X_{L_{f2}} - \hat{X}_{L_{f2}}(t))}{\mathcal{K}_{X_{f2}}} \\ - \frac{\dot{\tilde{V}}_{\text{PCC}_d}(t) (v_{\text{PCC}_d} - \hat{V}_{\text{PCC}_d}(t))}{\mathcal{K}_{v_{\text{PCC}_d}}} \\ - \frac{\dot{\tilde{V}}_{\text{PCC}_q}(t) (v_{\text{PCC}_q} - \hat{V}_{\text{PCC}_q}(t))}{\mathcal{K}_{v_{\text{PCC}_q}}}. \quad (26)$$

From (26), one reaches

$$\dot{V}_{\text{contr}}(t) = e_{i_{2d}}(t) (X_{L_{f2}} i_{2q}(t) - R_{t2} i_{2d}(t) - v_{\text{PCC}_d} \\ + u_{i_{2d}}(t) - L_{f2} \dot{i}_{2d\text{-ref}}(t)) \\ + e_{i_{2q}}(t) (-X_{L_{f2}} i_{2d}(t) - R_{t2} i_{2q}(t) - v_{\text{PCC}_q} \\ + u_{i_{2q}}(t) - L_{f2} \dot{i}_{2q\text{-ref}}(t)) \\ + (e_{i_{2d}}(t) \dot{i}_{2d\text{-ref}}(t) + e_{i_{2q}}(t) \dot{i}_{2q\text{-ref}}(t)) \\ (L_{f2} - \hat{L}_{f2}(t)) \\ + (e_{i_{2d}}(t) i_{2d}(t) + e_{i_{2q}}(t) i_{2q}(t)) (R_{t2} - \hat{R}_{t2}(t)) \\ - (e_{i_{2d}}(t) i_{2q}(t) - e_{i_{2q}}(t) i_{2d}(t)) (X_{L_{f2}} - \hat{X}_{L_{f2}}(t)) \\ + e_{i_{2d}}(t) (v_{\text{PCC}_d} - \hat{V}_{\text{PCC}_d}(t)) \\ + e_{i_{2q}}(t) (v_{\text{PCC}_q} - \hat{V}_{\text{PCC}_q}(t)). \quad (27)$$

Then, from (27), one obtains

$$\begin{aligned} \dot{V}_{\text{contr}}(t) &= e_{i_{2d}}(t) u_{i_{2d}}(t) + e_{i_{2q}}(t) u_{i_{2q}}(t) \\ &\quad - \hat{L}_{f2}(t) (e_{i_{2d}}(t) \dot{i}_{2d\text{-ref}}(t) + e_{i_{2q}}(t) \dot{i}_{2q\text{-ref}}(t)) \\ &\quad - \hat{R}_{t2}(t) (e_{i_{2d}}(t) i_{2d}(t) + e_{i_{2q}}(t) i_{2q}(t)) \\ &\quad + \hat{X}_{L_{f2}}(t) (e_{i_{2d}}(t) i_{2q}(t) - e_{i_{2q}}(t) i_{2d}(t)) \\ &\quad - \hat{V}_{\text{PCC}_d}(t) e_{i_{2d}}(t) \\ &\quad - \hat{V}_{\text{PCC}_q}(t) e_{i_{2q}}(t). \end{aligned} \quad (28)$$

Subsequently, by inserting the input signals of (23) into (28),  $\dot{V}_{\text{contr}}(t)$  is found as

$$\begin{aligned} \dot{V}_{\text{contr}}(t) &= -e_{i_{2d}}(t) k_{e_{i_{2d}}} \text{sign}(e_{i_{2d}}(t)) \\ &\quad -e_{i_{2q}}(t) k_{e_{i_{2q}}} \text{sign}(e_{i_{2q}}(t)). \\ \Rightarrow \quad \dot{V}_{\text{contr}}(t) &= -k_{e_{i_{2d}}} |e_{i_{2d}}(t)| - k_{e_{i_{2q}}} |e_{i_{2q}}(t)| \\ \Rightarrow \quad \dot{V}_{\text{contr}}(t) &< 0 \end{aligned} \quad (29)$$

Equation (29) completes the proof of *Theorem 2*. Consequently,  $i_{2d}$  tracks  $i_{2d\text{-ref}}$  (i.e.,  $i_{2d} \rightarrow i_{2d\text{-ref}}$ ) and  $i_{2q}$  tracks  $i_{2q\text{-ref}}$  (i.e.,  $i_{2q} \rightarrow i_{2q\text{-ref}}$ ), and hence,  $P_{\text{PCC}} \rightarrow P_{\text{PCC-ref}}$  and  $Q_{\text{PCC}} \rightarrow Q_{\text{PCC-ref}}$ , respectively. ■

#### IV. SIMULATIONS AND EXPERIMENTS

This section demonstrates the simulation results and experimental outcomes of the proposed methodology for different conditions that a GC-VSI may experience in grid integration in detail as follows. First, varieties of grid conditions are studied. In this regard, the first subsection considers integration into: 1) a strong, balanced grid; 2) an unbalanced grid (with a high short-circuit capacity compared to the capacity of the VSI), and 3) a weak grid, which are all covered in different subsubsections. Second, for comparison, the results of other methods targeting FSs removal from the GC-VSI's controls are introduced in order to reveal the superiority of the FSs rectifier proposed in this research. Last but not least, in order to show the practicality of the presented method, the third subsection reveals the experimental results of a GC-VSI prototype connected to the grid of Georgia Southern University.

This research sees the impact of FSs generated by attacks not detected by CPS-based power systems of MMGs. Therefore, FSs are required to show such emulations; the same type of changes have been considered in [18]–[25] as well. For all the test cases explained here, which are related to FSs' impacts on the control performance, 20% of the nominal values of  $\mathbf{y}$ 's arrays—according to the GC VSI's operating point—is added to  $\mathbf{y}$ 's arrays by the numbers that can be generated at any value but with a limited upper bound. Other researchers have also utilized almost the same type of testing in their simulations [18]–[25]. Here, those numbers are generated at any value—with

TABLE I  
PARAMETERS OF Fig. 3 EMPLOYED IN SECTION IV-A1, A2, AND B1 AND Fig. 14

Parameter	Value	Parameter	Value
$S_n^1$	10.81 kVA	SCC <sup>3</sup>	65 kVA
$L_{f1}/R_{f1}$	1.1 mH/0.01 $\Omega$	$L_{f2}/R_{f2}$	1.1 mH/0.01 $\Omega$
$C_f/R_f$	15.40 $\mu$ F/2.08 $\Omega$	$f_s^4$	8.1 kHz
$V_{DC}^2$	400 V	$V_{PCC, \text{Line-to-Line rms}}^2$	208 V
$\eta = \eta^P = \eta^N = \eta_{\text{new}}$	1	$\zeta = \zeta^P = \zeta^N$	1
$k_r = k_r^P = k_r^N = k_{\text{new}}$	1	$\mathcal{K}_{L_{f2}} = \mathcal{K}_{L_{f2}}^P = \mathcal{K}_{L_{f2}}^N$	200
$\mathcal{K}_{R_{t2}} = \mathcal{K}_{R_{t2}}^P = \mathcal{K}_{R_{t2}}^N$	200	$\mathcal{K}_{X_{f2}} = \mathcal{K}_{X_{f2}}^P = \mathcal{K}_{X_{f2}}^N$	200
$\mathcal{K}_{v_{PCCd}} = \mathcal{K}_{v_{PCCd}}^P = \mathcal{K}_{v_{PCCd}}^N$	200	$\mathcal{K}_{v_{PCCq}} = \mathcal{K}_{v_{PCCq}}^P = \mathcal{K}_{v_{PCCq}}^N$	200
$k_{e_{i2d}} = k_{e_{i2d}}^P = k_{e_{i2d}}^N$	2	$k_{e_{i2q}} = k_{e_{i2q}}^P = k_{e_{i2q}}^N$	2

<sup>1</sup> Nominal VA<sup>3</sup> PCC Short circuit capacity calculating  $Z_{\text{Grid}}$  [41]<sup>2</sup> Nominal value<sup>4</sup> Switching frequency

a limited upper bound—adding a dc average values to the output signals. In addition to them, sinusoidal waves (having limited amplitudes) are added to  $\mathbf{y}$ 's arrays. Different frequencies have been selected here—their angular frequencies are 500, 1000, 100, and 200 rad/s (or equivalently 79.578, 159.155, 15.916, and 31.831 Hz) for the first, second, third, and fourth array, respectively.

As the angular frequency of the fundamental frequency of electric power is either 60 or 50 Hz—which is approximately 377 or 314 rad/s, depending on the country—different angular frequencies that are higher and lower than the fundamental frequency have been considered. Therefore, two cases of 100 and 200 rad/s and two samples of 500 and 1000 rad/s—as the cases less and higher than the fundamental frequency—have been selected to be tested. Accordingly, the frequency of those are 79.578, 159.155, 15.916, and 31.831 Hz as per  $\omega = 2\pi \times f$ . It is worthy of note that the FSs have been added to the main feedback signals, which emulate a possible data integrity attack's behavior if CPS fails to prevent them. Indeed, they do “not” exist in the actual plant's dynamics, thereby exciting “no” resonant frequency to potentially pose a threat. All of the signals' attributes are selected to be generated at any value with a limited upper bound; they are able to emulate the FSs that can impact the signal by “any” value (with a limited upper bound) as much as possible.

#### A. Proposed Approach's Simulation Results in Different Grid Conditions

This subsection details the approach's results of the GC-VSI with the proposed FS rectifier. In order to make these simulations as comprehensive as possible, different grid conditions are considered and simulated.

1) *Balanced Grids With High Short-Circuit Capacity*: Here, balanced grids are taken into consideration. Fig. 3, whose parameters are given in Table I (with a balanced grid at PCC), has been simulated using the Simulink in MATLAB as the GC-VSI elaborated in this article. The FSs have been emulated via different signals manipulating the output vector of  $\mathbf{y}$ ; they have been explained before Section IV-A. This manipulation can happen by “any” amplitude with a limited upper bound. Those signals are designed to consider several possible cases

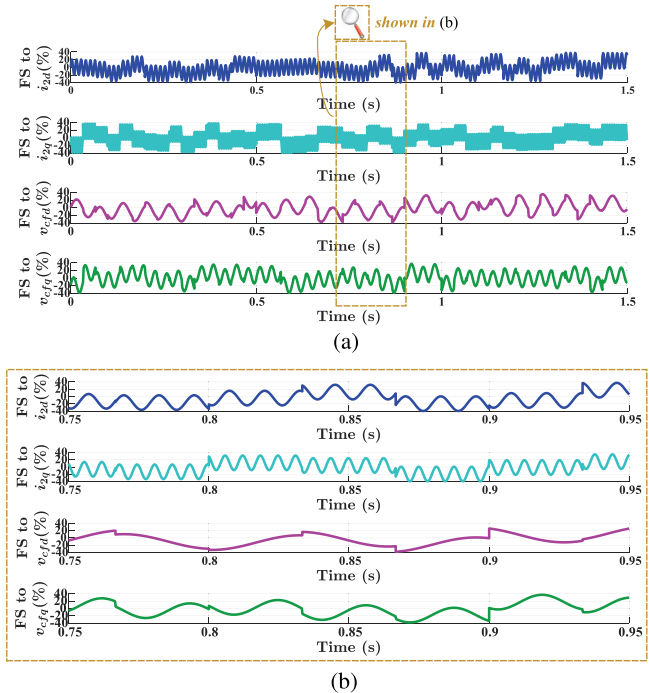


Fig. 5. FSs (created by cyber threats, sensor faults, and so forth) impacting the output of  $\mathbf{y}$  in Fig. 3 ( $i_{2d}$ ,  $i_{2q}$ ,  $v_{cfq}$ , and  $v_{cfq}$ , from the top graph to the bottom one). (a) Whole time window. (b) Enlarged view of Fig. 5(a).

(i.e., various “dc average” values and different frequencies), as detailed below.

a) *Test case*: The examined test case is described as follows. Fig. 5 shows the emulated FSs on the signals of interest, which are  $i_{2d}$ ,  $i_{2q}$ ,  $v_{cfq}$ , and  $v_{cfq}$ , from the top graph to the bottom one, respectively. In Fig. 5, FS samples impacting  $\mathbf{y}$ 's arrays are demonstrated in different colors and in percentage. The percentage calculations are based on the  $\mathbf{y}$ 's arrays' values of the GC-VSI's operating point. The whole and enlarged graphs in Fig. 5 show that the dc average of the signals is changing, and the amplitude of sinusoidal waves is altered by any number (with a limited value). In order to examine the proposed FC rectifier—while FSs of Fig. 5 are in place—the test case shown in Fig. 6 is conducted. The outcomes have been discussed below.

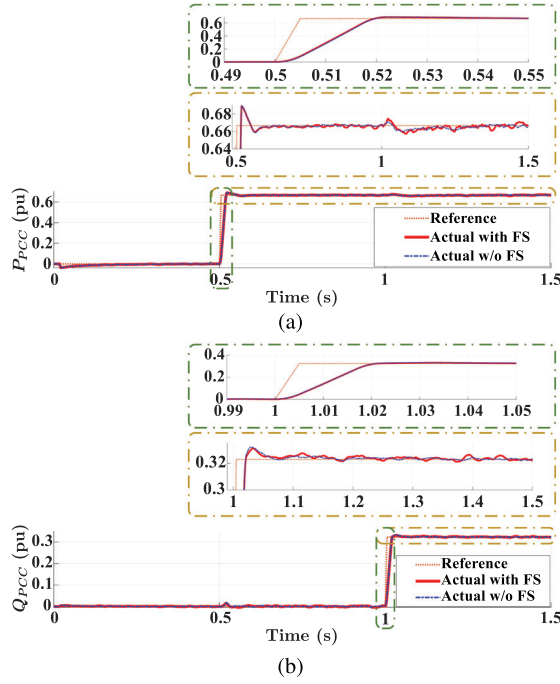


Fig. 6. Simulation of Fig. 3 connected to a balanced grid with high short-circuit capacity detailed in Section IV-A1 with the controller of Fig. 4. (a) Active power of  $P_{PCC}$  injected into PCC with/without FS. (b) Reactive power of  $Q_{PCC}$  injected into PCC with/without FS.

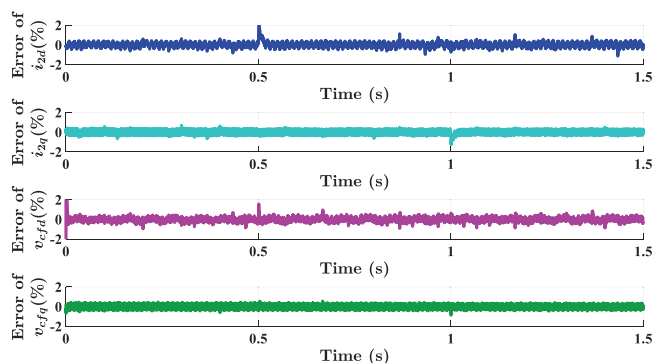


Fig. 7. Error between the rectified signals (generated by the sliding-mode-based FS rectifier) and the same signals "without" FSs for  $y$ 's arrays, i.e.,  $i_{2d}$ ,  $i_{2q}$ ,  $v_{cfd}$ , and  $v_{cfq}$  from the top to the bottom, respectively.

*b) Discussions about the results:* First, both active power and reactive power are set zero. Next, at  $t = 0.5$  s, the reference signal of active power  $P_{PCC}$  is set to 0.6 pu. Afterward, at  $t = 1.0$  s, the reactive power  $Q_{PCC}$  is set to 0.3 pu while the other condition still exists. Fig. 6 has depicted the active/reactive power—which includes the references and actual signals with and without FS. Last but not least, in order to check the effectiveness of the proposed sliding-mode-based FS rectifier, Fig. 7 depicts the error between rectified signals and without-faulty-signal  $y$ 's arrays, i.e.,  $i_{2d}$ ,  $i_{2q}$ ,  $v_{cfd}$ , and  $v_{cfq}$  (from the top graph to the bottom one), respectively. It shows the errors in percentage based on the  $y$ 's arrays' values of the GC-VSI's operating point. As shown in Figs. 6 and 7, the proposed FS rectifier is able to

rectify the signals while incorporated into the primary control (also known as zero-level control) and rigorously stabilize  $P_{PCC}$  and  $Q_{PCC}$  to their reference signals. It is worthy of note that the control in this level is the most inner loop, whose time constant is the fastest among all control levels in the hierarchical structure of the MMGs. Therefore, as noted in the introduction, if the CPS cannot prevent any issues from happening that come into the primary control, the system itself is able to survive and operate until further actions take place in the CPS-based MMG.

*2) Unbalanced Grids With High Short-Circuit Capacity:* Here, unbalanced grids are considered. As this research's scope is not merely focusing on proposing controllers for GC-VSI's integration into unbalanced grids, the commonly used dual current control scheme for PWM-based VSIs under unbalanced input voltage conditions have been employed [42]. It is a simple yet powerful control, which is also industrially accepted for such a situation. In that scheme, the instantaneous power fluctuates with the double frequency as described in (30) and (31) [42]; also, two dynamics exist that are linked to each of the positive sequence and the negative one, individually [42]

$$\begin{cases} p(t) = P_0 + P_{\cos} \cos(2\omega t) + P_{\sin} \sin(2\omega t) \\ q(t) = Q_0 + Q_{\cos} \cos(2\omega t) + Q_{\sin} \sin(2\omega t) \end{cases} \quad (30)$$

where

$$\begin{cases} P_0 \triangleq 1.50(v_{PCCd}^P i_{2d}^P + v_{PCCq}^P i_{2q}^P + v_{PCCd}^N i_{2d}^N + v_{PCCq}^N i_{2q}^N) \\ P_{\cos} \triangleq 1.50(v_{PCCd}^P i_{2d}^N + v_{PCCq}^P i_{2q}^N + v_{PCCd}^N i_{2d}^P + v_{PCCq}^N i_{2q}^P) \\ P_{\sin} \triangleq 1.50(v_{PCCq}^N i_{2d}^P - v_{PCCd}^N i_{2q}^P - v_{PCCq}^P i_{2d}^N + v_{PCCd}^P i_{2q}^N) \end{cases} \quad (31a)$$

$$\begin{cases} Q_0 \triangleq 1.50(v_{PCCq}^P i_{2d}^P - v_{PCCd}^P i_{2q}^P + v_{PCCq}^N i_{2d}^N - v_{PCCd}^N i_{2q}^N) \\ Q_{\cos} \triangleq 1.50(v_{PCCq}^P i_{2d}^N - v_{PCCd}^P i_{2q}^N + v_{PCCq}^N i_{2d}^P - v_{PCCd}^N i_{2q}^P) \\ Q_{\sin} \triangleq 1.50(v_{PCCd}^P i_{2d}^N + v_{PCCq}^P i_{2q}^N - v_{PCCd}^N i_{2d}^P - v_{PCCq}^N i_{2q}^P) \end{cases} \quad (31b)$$

As a result, equations (22) and (23) should be updated by (32)/(33) and (34)/(35), respectively, for each of the positive and negative sequences. The rationale for this update is that Theorem 2 has already proved the positive sequence's closed-loop dynamics' stability. Thus, the same FS rectifier can be employed in each sequence's dynamics as they share the same dynamics except for the angular frequency which is "negative" in the negative sequence. The FS rectifier's proposed structure has been applied in rectifying each sequence outputs to be embedded into individual sequence's dynamics separately. Fig. 8 has depicted the described system

$$\begin{cases} \dot{\hat{L}}_{f2}^P(t) = -\mathcal{K}_{L_{f2}}^P (e_{i_{2d}^P}(t) i_{2d-\text{ref}}^P(t) + e_{i_{2q}^P}(t) i_{2q-\text{ref}}^P(t)) \\ \dot{\hat{R}}_{f2}^P(t) = -\mathcal{K}_{R_{f2}}^P (e_{i_{2d}^P}(t) i_{2d}^P(t) + e_{i_{2q}^P}(t) i_{2q}^P(t)) \\ \dot{\hat{X}}_{f2}^P(t) = +\mathcal{K}_{X_{f2}}^P (e_{i_{2d}^P}(t) i_{2q}^P(t) - e_{i_{2q}^P}(t) i_{2d}^P(t)) \\ \dot{\hat{V}}_{PCCd}^P(t) = -\mathcal{K}_{v_{PCCd}}^P e_{i_{2d}^P}(t) \\ \dot{\hat{V}}_{PCCq}^P(t) = -\mathcal{K}_{v_{PCCq}}^P e_{i_{2q}^P}(t) \end{cases} \quad (32)$$

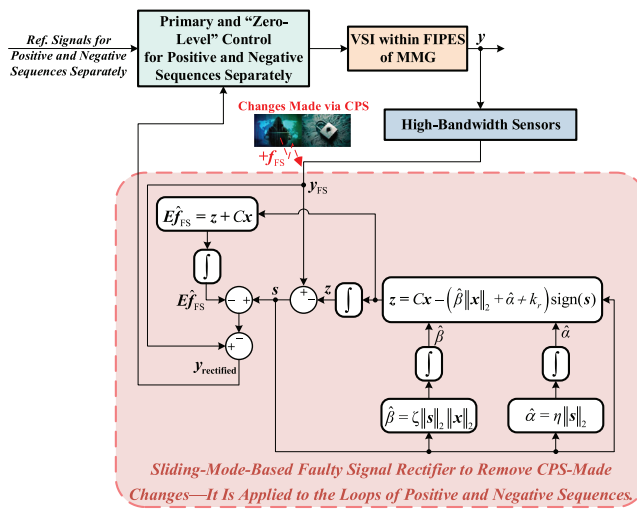


Fig. 8. Proposed faulty-signal-tolerant control for GC-VSIs integrated into unbalanced grids.

and

$$\begin{cases} \dot{\hat{L}}_{f2}^N(t) = -\mathcal{R}_{L_{f2}}^N \left( e_{i_{2d}^N}(t) \dot{i}_{2d\text{-ref}}^N(t) + e_{i_{2q}^N}(t) \dot{i}_{2q\text{-ref}}^N(t) \right) \\ \dot{\hat{R}}_{t2}^N(t) = -\mathcal{R}_{R_{t2}}^N \left( e_{i_{2d}^N}(t) \dot{i}_{2d}^N(t) + e_{i_{2q}^N}(t) \dot{i}_{2q}^N(t) \right) \\ \dot{\hat{X}}_{f2}^N(t) = -\mathcal{R}_{X_{f2}}^N \left( e_{i_{2d}^N}(t) \dot{i}_{2q}^N(t) - e_{i_{2q}^N}(t) \dot{i}_{2d}^N(t) \right) \\ \dot{\hat{V}}_{PCCd}^N(t) = -\mathcal{R}_{v_{PCCd}}^N e_{i_{2d}^N}(t) \\ \dot{\hat{V}}_{PCCq}^N(t) = -\mathcal{R}_{v_{PCCq}}^N e_{i_{2q}^N}(t) \end{cases} \quad (33)$$

where  $\mathcal{R}_{L_{f2}}^P$ ,  $\mathcal{R}_{R_{t2}}^P$ ,  $\mathcal{R}_{X_{f2}}^P$ ,  $\mathcal{R}_{v_{PCCd}}^P$ ,  $\mathcal{R}_{v_{PCCq}}^P$ ,  $\mathcal{R}_{L_{f2}}^N$ ,  $\mathcal{R}_{R_{t2}}^N$ ,  $\mathcal{R}_{X_{f2}}^N$ ,  $\mathcal{R}_{v_{PCCd}}^N$ , and  $\mathcal{R}_{v_{PCCq}}^N$  are all positive values, and  $e_{i_{2d}^P} \triangleq i_{2d}^P - i_{2d\text{-ref}}$ ,  $e_{i_{2q}^P} \triangleq i_{2q}^P - i_{2q\text{-ref}}$ ,  $e_{i_{2d}^N} \triangleq i_{2d}^N - i_{2d\text{-ref}}$ , and  $e_{i_{2q}^N} \triangleq i_{2q}^N - i_{2q\text{-ref}}$ . Also, the initial values of the functions above are the positive, nominal values of  $L_{f2}$ ,  $R_{t2}$ ,  $X_{f2} \triangleq \omega_0 L_{f2}$  (i.e., the nominal impedance of  $L_{f2}$  at the nominal frequency of  $\omega_0$ ),  $v_{PCCd}$ , and  $v_{PCCq}$ , respectively

$$\begin{cases} u_{i_{2d}^P}(t) = \hat{R}_{t2}^P(t) i_{2d}^P - \hat{X}_{L_{f2}}^P(t) i_{2q}^P + \hat{V}_{PCCd}^P(t) \\ \quad + \hat{L}_{f2}^P(t) \dot{i}_{2d\text{-ref}}^P - k_{e_{i_{2d}^P}}^P \text{sign}(e_{i_{2d}^P}(t)) \\ u_{i_{2q}^P}(t) = \hat{R}_{t2}^P(t) i_{2q}^P + \hat{X}_{L_{f2}}^P(t) i_{2d}^P + \hat{V}_{PCCq}^P(t) \\ \quad + \hat{L}_{f2}^P(t) \dot{i}_{2q\text{-ref}}^P - k_{e_{i_{2q}^P}}^P \text{sign}(e_{i_{2q}^P}(t)) \end{cases} \quad (34)$$

and

$$\begin{cases} u_{i_{2d}^N}(t) = \hat{R}_{t2}^N(t) i_{2d}^N + \hat{X}_{L_{f2}}^N(t) i_{2q}^N + \hat{V}_{PCCd}^N(t) \\ \quad + \hat{L}_{f2}^N(t) \dot{i}_{2d\text{-ref}}^N - k_{e_{i_{2d}^N}}^N \text{sign}(e_{i_{2d}^N}(t)) \\ u_{i_{2q}^N}(t) = \hat{R}_{t2}^N(t) i_{2q}^N - \hat{X}_{L_{f2}}^N(t) i_{2d}^N + \hat{V}_{PCCq}^N(t) \\ \quad + \hat{L}_{f2}^N(t) \dot{i}_{2q\text{-ref}}^N - k_{e_{i_{2q}^N}}^N \text{sign}(e_{i_{2q}^N}(t)) \end{cases} \quad (35)$$

where  $k_{e_{i_{2d}^P}}^P$ ,  $k_{e_{i_{2q}^P}}^P$ ,  $k_{e_{i_{2d}^N}}^N$ , and  $k_{e_{i_{2q}^N}}^N$  are positive numbers.

*Remark 4:* One is able to prove that (34) and (35) also stabilize the closed-loop systems associated with two sequences under investigation. This proof needs to proceed with what has been provided for Theorem 2. It has already inferred that

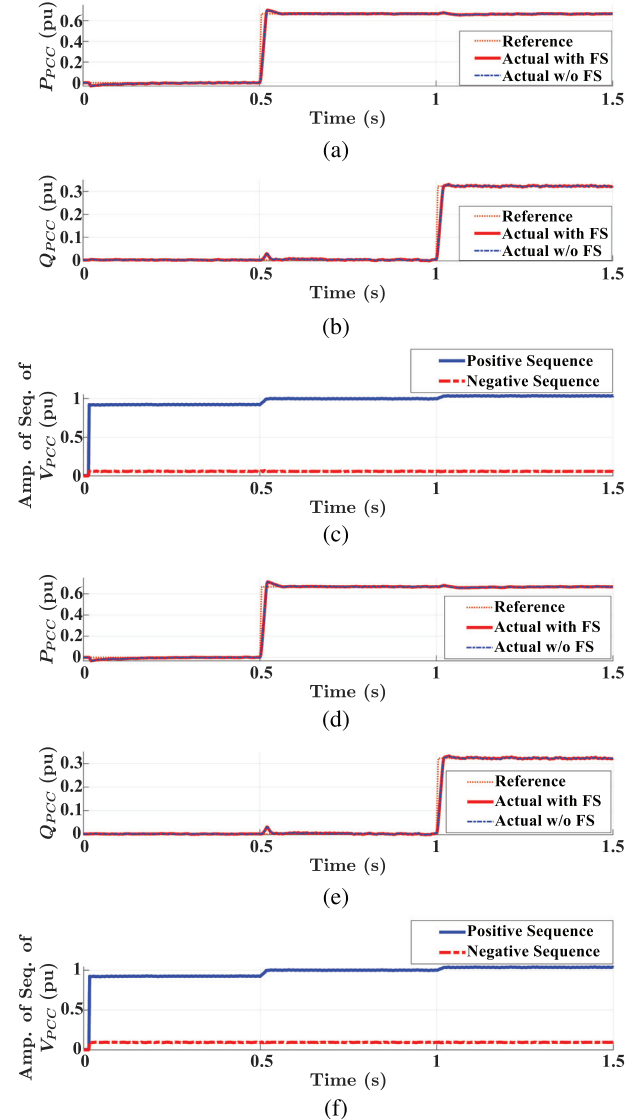


Fig. 9. Simulation of Fig. 3 connected to an unbalanced grid with high short-circuit capacity with the controller detailed in Section IV-A2; the first test case (Phase A is 1.00 pu, Phase B is 0.90 pu, and Phase C is 0.80 pu). (a) Active power of  $P_{PCC}$  injected into PCC with/without FS. (b) Reactive power of  $Q_{PCC}$  injected into PCC with/without FS. (c) Positive and negative sequence of  $V_{PCC}$ ; and the second test case (Phase A is 1.00 pu, Phase B is 0.85 pu, and Phase C is 0.70 pu). (d) Active power of  $P_{PCC}$  injected into PCC with/without FS. (e) Reactive power of  $Q_{PCC}$  injected into PCC with/without FS. (f) Positive and negative sequence of  $V_{PCC}$ .

(34) stabilizes the positive sequence's closed-loop dynamics. Likewise, the same proof procedure concludes so for the negative sequence's ones.

Fig. 3, whose parameters have been reported in Table I (with unbalanced PCC voltages described below), has been simulated as detailed in Section IV-A1. Here, two unbalanced grids have been considered as follows. In the first unbalanced test case, the voltage of Phase B is reduced to 90% while that of Phase C is reduced to 80%. The results of the simulation conditions as those in Section IV-A1 have been shown in Fig. 9(a)–(c). In the second unbalanced test case, the voltage of Phase B is reduced

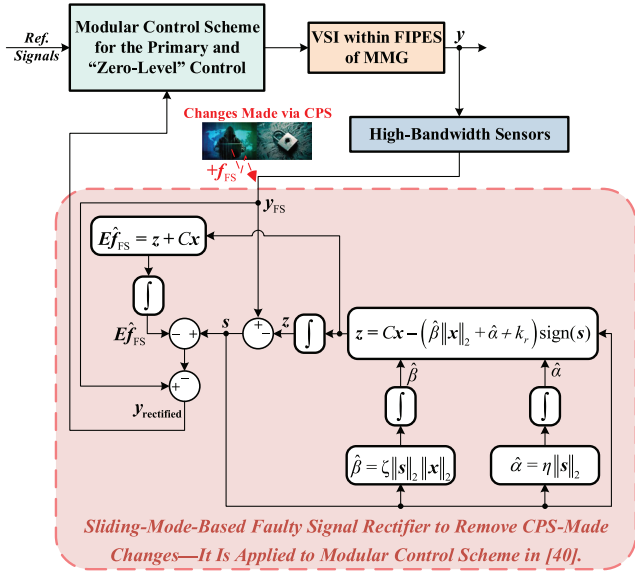


Fig. 10. Proposed faulty-signal-tolerant control for GC-VSIs integrated into weak grids.

to 85% while that of Phase C is reduced to 70%. The results of the simulation conditions as those in Section IV-A1 have been shown in Fig. 9(d)–(f).

3) *Weak Grids*: Here, weak grids are taken into account. Regarding weak grids, many considerations affect weak-grid integration. They are: 1) The impedance of the grid (which impacts the short-circuit capacity of the PCC); 2) the type of the grid impedance (considered by the ratio of  $X_{\text{Grid}}/R_{\text{Grid}}$ ); 3) the inertia of the grid at the PCC; and 4) last but not least, the PLL controller [40], [43]. Each of them should be tackled individually. As [40] introduces one of the possible methods, it takes care of each of them through separate modules in a modular control structure. It is worthy of note that designing a novel controller for weak-grid integration is not part of this article's principal scopes. Then, the synthesized FS rectifier is embedded in one of its controls (detailed in [40]) to show the performance of this article's proposed system in weak-grid integration. Therefore, the proposed structure of the FS rectifier has been applied in the modular control structure discussed in [40]. Fig. 10 has shown the discussed structure.

Fig. 3, whose parameters have been given with a weak grid at the PCC detailed in [40], has been simulated considering the FSs described in Section IV-A1. The control structure proposed in [40] is enhanced by the FS rectifier introduce herein. Also, two test cases have been simulated in order to examine its performance. Here, Test Cases I and II described in [40] have been simulated. Test Case I deals with high reactive power variation and low active power change at the beginning. Afterward, the power factor (PF) is changed from 0.95 to 1.0 at  $t = 1.5$  s, and the active power is varied from 0.5 to 1.00 pu at  $t = 3.0$  s. The grid has been simulated for the worst case of weak-grid conditions, i.e., short-circuit capacity ratio (SCCR) equals to 1 and inertia constant of  $H = 1$ . Test Case II considers high active power change and low reactive power variation at the beginning.

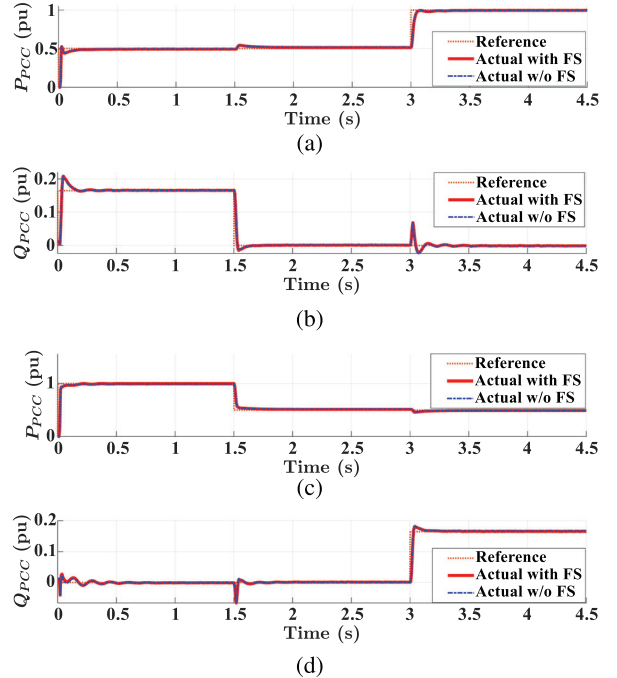


Fig. 11. Simulation of Fig. 3 connected to a weak grid with the controller detailed in Section IV-A3; Test Case I. (a) Active power of  $P_{PCC}$  injected into PCC with/without FS. (b) Reactive power of  $Q_{PCC}$  injected into PCC with/without FS; and Test Case II: (c) Active power of  $P_{PCC}$  injected into PCC with/without FS. (d) Reactive power of  $Q_{PCC}$  injected into PCC with/without FS.

Afterward, in Test Case II, the active power is varied from 1.0 to 0.5 pu at  $t = 1.5$  s, and the PF is altered from 1.0 to 0.95 at  $t = 3.0$  s again for  $\text{SCCR} = 1$  and  $H = 1$ . The results of Test Case I with the introduced FS rectifier have been shown in Fig. 11(a)–(b), and those of Test Case II using the discussed FS rectifier have been depicted in Fig. 11(c)–(d). Other signals, e.g., frequency, voltage signals, and so on, can be found in Figs. 4–7 in [40].

### B. Comparative Results of Other Approaches

This subsection demonstrates comparative simulations. They show the GC-VSI using a different FS rectifier and a sliding-mode-based fault observer. In order to make this comparison, first, a similar design with less sophisticated adaptive dynamics is designed in detail, and its outcomes have been depicted. Second, another approach, which uses a conventional proportional-integral-based (PI-based) controller in  $dq$ -frame augmented with another sliding-mode-based fault observer, has briefly described. Its results have been shown. Hereinafter, the former is named "Method #1," while the latter is called "Method #2," as discussed below.

1) *Method #1*: In this subsubsection, the proposed FS rectifier is designed, but with less information involved in the dynamics of the adaptive dynamics detailed in (9).

Now, an adaptive FS identifier for the system of (5) is synthesized. First, the vector of sliding surface  $s$  and an auxiliary variable  $z$  are defined as

$$s_{\text{new}} = z_{\text{new}} - y, \Rightarrow s_{\text{new}} = z_{\text{new}} - Cx - Ef_{\text{FS}}$$

$$\Rightarrow \mathbf{E}\dot{\mathbf{f}}_{\text{FS}} = \mathbf{z}_{\text{new}} - \mathbf{C}\dot{\mathbf{x}} - \dot{\mathbf{s}}_{\text{new}}.$$

Therefore,  $\dot{\mathbf{s}}_{\text{new}} = \dot{\mathbf{z}}_{\text{new}} - \dot{\mathbf{y}}$ ,  $\Rightarrow \dot{\mathbf{s}}_{\text{new}} = \dot{\mathbf{z}}_{\text{new}} - \mathbf{C}\dot{\mathbf{x}} - \mathbf{E}\dot{\mathbf{f}}_{\text{FS}}$

$$\Rightarrow \mathbf{E}\dot{\mathbf{f}}_{\text{FS}} = \dot{\mathbf{z}}_{\text{new}} - \mathbf{C}\dot{\mathbf{x}} - \dot{\mathbf{s}}_{\text{new}}. \quad (36)$$

Now, supposing  $\|\mathbf{E}\dot{\mathbf{f}}_{\text{FS}}\|_2 \leq \alpha_{\text{new}}$ , where  $\alpha_{\text{new}} > 0$  is an unknown constant, we define “new” adaptive dynamics as

$$\begin{cases} \dot{\mathbf{z}}_{\text{new}} = \mathbf{C}\dot{\mathbf{x}} - (k_{\text{new}} + \hat{\alpha}_{\text{new}})\text{sign}(\mathbf{s}_{\text{new}}) \\ \dot{\hat{\alpha}}_{\text{new}} = \eta_{\text{new}}\|\mathbf{s}_{\text{new}}\|_2 \end{cases} \quad (37)$$

where  $k_{\text{new}} > 0$  and  $\eta_{\text{new}} > 0$  are constants.

The theorem below proves that the adaptive dynamics of (9) are stable, as shown in the following theorem.

*Theorem 3 (Stability of the “newly” designed FS rectifier):* Consider the uncertain system of (5) along with the auxiliary variables of  $\mathbf{s}_{\text{new}}$  and  $\mathbf{z}_{\text{new}}$  defined above. The origin is the stable equilibrium point of the adaptive dynamical FS “rectifier” of (37).

*Proof:* The Lyapunov function of  $V_{\text{rect-new}}(t)$  is defined as

$$V_{\text{rect-new}}(t) = \frac{1}{2}\|\mathbf{s}_{\text{new}}\|_2^2 + \frac{1}{2\eta_{\text{new}}}\hat{\alpha}_{\text{new}}^2 \quad (38)$$

where  $\tilde{\alpha}_{\text{new}} \triangleq \alpha_{\text{new}} - \hat{\alpha}_{\text{new}}$ .

From (38)

$$\dot{V}_{\text{rect-new}}(t) = \mathbf{s}_{\text{new}}^T \dot{\mathbf{s}}_{\text{new}} - \frac{\dot{\hat{\alpha}}_{\text{new}}}{\eta_{\text{new}}}(\alpha_{\text{new}} - \hat{\alpha}_{\text{new}}). \quad (39)$$

From (36) and (37), (39) is expressed as

$$\begin{aligned} \dot{V}_{\text{rect-new}}(t) &= \mathbf{s}_{\text{new}}^T (\dot{\mathbf{z}}_{\text{new}} - \mathbf{C}\dot{\mathbf{x}} - \mathbf{E}\dot{\mathbf{f}}_{\text{FS}}) \\ &\quad - \|\mathbf{s}_{\text{new}}\|_2(\alpha_{\text{new}} - \hat{\alpha}_{\text{new}}). \end{aligned} \quad (40)$$

As a result, (37) and (40) conclude

$$\begin{aligned} \dot{V}_{\text{rect-new}}(t) &\leq \mathbf{s}_{\text{new}}^T (\dot{\mathbf{z}}_{\text{new}} - \mathbf{C}\dot{\mathbf{x}}) + \|\mathbf{s}_{\text{new}}\|_2 \|\mathbf{E}\dot{\mathbf{f}}_{\text{FS}}\|_2 \\ &\quad - \|\mathbf{s}_{\text{new}}\|_2(\alpha_{\text{new}} - \hat{\alpha}_{\text{new}}) \\ \Rightarrow \dot{V}_{\text{rect-new}}(t) &\leq \mathbf{s}_{\text{new}}^T (-(k_{\text{new}} + \hat{\alpha}_{\text{new}})\text{sign}(\mathbf{s}_{\text{new}})) + \alpha \|\mathbf{s}\|_2 \\ &\quad - \|\mathbf{s}_{\text{new}}\|_2(\alpha_{\text{new}} - \hat{\alpha}_{\text{new}}). \end{aligned} \quad (41)$$

From (14) and by using  $\mathbf{s}^T \text{sign}(\mathbf{s}) = \|\mathbf{s}\|_1$ , the upper bound of  $\dot{V}_{\text{rect-new}}(t)$  is described as

$$\begin{aligned} \dot{V}_{\text{rect-new}}(t) &\leq -(k_{\text{new}} + \hat{\alpha}_{\text{new}})\|\mathbf{s}_{\text{new}}\|_1 \\ &\quad + \|\mathbf{s}_{\text{new}}\|_2 \hat{\alpha}_{\text{new}} \\ \Rightarrow \dot{V}_{\text{rect-new}}(t) &\leq -k_{\text{new}}\|\mathbf{s}_{\text{new}}\|_1 \\ &\quad - \underbrace{\hat{\alpha}_{\text{new}}\|\mathbf{s}_{\text{new}}\|_1 + \|\mathbf{s}_{\text{new}}\|_2 \hat{\alpha}_{\text{new}}}_{\text{A Negative Term}}. \end{aligned} \quad (42)$$

Inequality (15)—considering  $\|\mathbf{s}_{\text{new}}\|_2 \leq \|\mathbf{s}_{\text{new}}\|_1$ —concludes  $\dot{V}_{\text{rect-new}}(t) < 0$ . Therefore, the proof is completed.

*Corollary 3 (Estimation of the FS using new estimator):* The vector of  $\mathbf{E}\dot{\mathbf{f}}_{\text{FS}}$  is defined as  $\mathbf{E}\dot{\mathbf{f}}_{\text{FS}} \triangleq \dot{\mathbf{z}}_{\text{new}} + \mathbf{C}\dot{\mathbf{x}}$ , where  $\dot{\mathbf{f}}_{\text{FS}}$  is defined as an estimation of the FS vector of  $\mathbf{f}_{\text{FS}}$ . By defining  $\tilde{\mathbf{f}}_{\text{FS}}$  as the FS error vector, one can prove that  $\tilde{\mathbf{f}}_{\text{FS}}$  reaches  $\mathbf{0}$  as

$t \rightarrow \infty$  (i.e.,  $\tilde{\mathbf{f}}_{\text{FS}} \rightarrow \mathbf{0}$  as  $t \rightarrow \infty$ ), or equivalently  $\dot{\mathbf{f}}_{\text{FS}}$  reaches  $\mathbf{f}_{\text{FS}}$  (i.e.,  $\dot{\mathbf{f}}_{\text{FS}} \rightarrow \mathbf{f}_{\text{FS}}$ ) as  $t \rightarrow \infty$ .

*Proof:* Now,  $\mathbf{E}\dot{\mathbf{f}}_{\text{FS}}$  is defined as

$$\mathbf{E}\dot{\mathbf{f}}_{\text{FS}} \triangleq \dot{\mathbf{z}}_{\text{new}} + \mathbf{C}\dot{\mathbf{x}}. \quad (43)$$

In (43),  $\dot{\mathbf{f}}_{\text{FS}}$  is defined as an estimation of the FS  $\mathbf{f}_{\text{FS}}$ . By defining  $\dot{\mathbf{f}}_{\text{FS}}$  as the fault error

$$\tilde{\mathbf{f}}_{\text{FS}} = \dot{\mathbf{f}}_{\text{FS}} - \mathbf{f}_{\text{FS}}, \Rightarrow \mathbf{E}\dot{\mathbf{f}}_{\text{FS}} = \mathbf{E}\dot{\mathbf{f}}_{\text{FS}} - \mathbf{E}\dot{\mathbf{f}}_{\text{FS}}. \quad (44)$$

Equations (44) and (43) conclude

$$\mathbf{E}\dot{\mathbf{f}}_{\text{FS}} = \dot{\mathbf{z}}_{\text{new}} + \mathbf{C}\dot{\mathbf{x}} - \dot{\mathbf{f}}_{\text{FS}}. \quad (45)$$

Also, from (5),  $\mathbf{E}\dot{\mathbf{f}} = \dot{\mathbf{y}} - \mathbf{C}\dot{\mathbf{x}}$  is obtained. Consequently

$$\mathbf{E}\dot{\mathbf{f}}_{\text{FS}} = \dot{\mathbf{z}} + \mathbf{C}\dot{\mathbf{x}} - (\dot{\mathbf{y}} - \mathbf{C}\dot{\mathbf{x}}) = \dot{\mathbf{z}} - \dot{\mathbf{y}}. \quad (46)$$

Considering the definition of  $\mathbf{s}$  (i.e.,  $\mathbf{s}_{\text{new}} \triangleq \mathbf{z}_{\text{new}} - \mathbf{y}$ ), (46) becomes  $\mathbf{E}\dot{\mathbf{f}}_{\text{FS}} = \dot{\mathbf{z}}_{\text{new}} - \dot{\mathbf{y}} = \dot{\mathbf{s}}_{\text{new}}$ .

As a consequence, according to Theorem 3, since  $\mathbf{s}$  reaches zero (i.e.,  $\mathbf{s}_{\text{new}} \rightarrow \mathbf{0}$ ) as  $t$  goes infinity (i.e.,  $t \rightarrow \infty$ )—based on Barbalat’s Lemma [36]—and since  $\|\mathbf{E}\dot{\mathbf{f}}_{\text{FS}}\|_2$  and  $\|\mathbf{E}\dot{\mathbf{f}}\|_2$  are bounded, it is concluded that  $\dot{\mathbf{f}}_{\text{FS}} \rightarrow \mathbf{0}$  as  $t \rightarrow \infty$ . Therefore,  $\tilde{\mathbf{f}}_{\text{FS}} \rightarrow \mathbf{f}_{\text{FS}}$  as  $t \rightarrow \infty$ , which concludes the proof.

*Remark 5:* As proved in Corollary 2, it similarly concludes that the uncertain system of (5) can be controlled by any currently stabilizing output feedback controller for the VSI considering the stable sliding-mode-based FS rectifier of the adaptive dynamics of (37) and referring to Fig. 4.

The discussed control structure with the newly designed FS rectifier described above has been used in Fig. 3, whose parameters have been provided in Table I. It has been simulated as detailed in Section IV-A1. The results of the test cases used in this research have been shown in Fig. 12(a)–(b). As they have shown, the system’s performance worsens in the presence of the FSs made in this research. This matter happens because of the interaction of the FS rectifier and controller. Looking at (9) and (37)—and comparing them—this poor performance could be expected since the impact of state vector’s norm (and its unknown upper bound) has not been seen in Method #1.

2) *Method #2:* This subsubsection discusses one of the common designs based on the sliding mode observer of fault. It also uses the typical PI-based control structure with the decoupling and feed-forward signals in the  $dq$ -frame. As shown in [21], the authors have benefited from such an approach, whose sliding-mode-based fault observer has been briefly described below.

Let us assume that the “filtered” signal of the measured output  $\mathbf{y}$  [described in (5)] can be written as follows:

$$\dot{\mathbf{x}}_f = -\mathbf{A}_f \mathbf{x}_f + \mathbf{A}_f \mathbf{y}, \quad (47)$$

where  $-\mathbf{A}_f$  denotes a diagonal positive definite matrix where time constants of the filter are inverse of the diagonal elements, and  $-\mathbf{A}_f$  is a stable matrix. In (47), the filter is stable. As a consequence, the augmented state-space representation of the

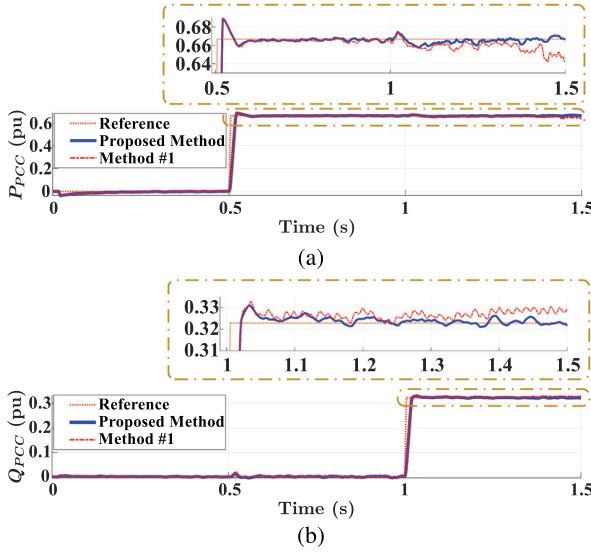


Fig. 12. Simulation of Fig. 3 connected to a balanced grid with high short-circuit capacity using Method #1 detailed in Section IV-B1. (a) Active power of  $P_{PCC}$  injected into PCC with/without FS. (b) Reactive power of  $Q_{PCC}$  injected into PCC with/without FS.

system is

$$\begin{cases} \dot{\mathbf{x}}_{\text{aug}} = \mathbf{A}_{\text{aug}} \mathbf{x}_{\text{aug}} + \mathbf{B}_{\text{aug}} \mathbf{u}_{\text{aug}} + \mathbf{E}_{\text{aug}} \mathbf{f}_{\text{FS}} \\ \mathbf{y} = \mathbf{C}_{\text{aug}} \mathbf{x}_{\text{aug}} \end{cases} \quad (48)$$

$$\text{where } \mathbf{x}_{\text{aug}} = \begin{bmatrix} \mathbf{x} \\ \mathbf{x}_f \end{bmatrix}, \mathbf{u}_{\text{aug}} = \begin{bmatrix} \mathbf{u} \\ \mathbf{d} \end{bmatrix}$$

$$\mathbf{A}_{\text{aug}} = \begin{bmatrix} \mathbf{A} & 0 \\ \mathbf{A}_f \mathbf{C} & -\mathbf{A}_f \end{bmatrix} \quad (49)$$

$$\mathbf{B}_{\text{aug}} = \begin{bmatrix} \mathbf{B}_1 & \mathbf{B}_2 \\ 0 & 0 \end{bmatrix} \quad (50)$$

$$\mathbf{C}_{\text{aug}} = \begin{bmatrix} 0 & \mathbf{I} \end{bmatrix} \text{ and} \quad (51)$$

$$\mathbf{E}_{\text{aug}} = \begin{bmatrix} 0 \\ \mathbf{A}_f \mathbf{E} \end{bmatrix}. \quad (52)$$

Therefore, the following fault observer can be designed

$$\begin{cases} \dot{\mathbf{x}}_{\text{obs}} = \mathbf{A}_{\text{aug}} \mathbf{x}_{\text{obs}} + \mathbf{B}_{\text{aug}} \mathbf{u}_{\text{aug}} - \mathbf{G}_l \mathbf{e}_{\text{out}} + \mathbf{G}_n \nu \\ \mathbf{y}_{\text{aug}} = \mathbf{C}_{\text{aug}} \mathbf{x}_{\text{obs}} \end{cases} \quad (53)$$

where  $\mathbf{x}_{\text{obs}}$  is fault observer's state, and

$$\nu = \begin{cases} -\gamma \frac{\mathbf{M}_0 \mathbf{e}_{\text{out}}}{\|\mathbf{M}_0 \mathbf{e}_{\text{out}}\|}, & \text{if } \mathbf{e}_{\text{out}} > 0 \\ 0, & \text{otherwise.} \end{cases} \quad (54)$$

In (54),  $\mathbf{e}_{\text{out}}$  is the output estimation error,  $\mathbf{M}_0$  is a symmetric positive definite matrix with appropriate size and  $\gamma$  is an upper bound on  $\|\mathbf{f}_{\text{FS}}\|_2$ . The matrix  $\mathbf{G}_l$  is the gain of traditional Luenberger observer, which makes  $(\mathbf{A}_{\text{aug}} - \mathbf{G}_l \mathbf{C}_{\text{aug}})$  stable.  $\mathbf{G}_n$  is the gain of the discontinuous function of  $\nu$  in (54). The authors in [44]–[46] have shown that sliding mode observer of the form

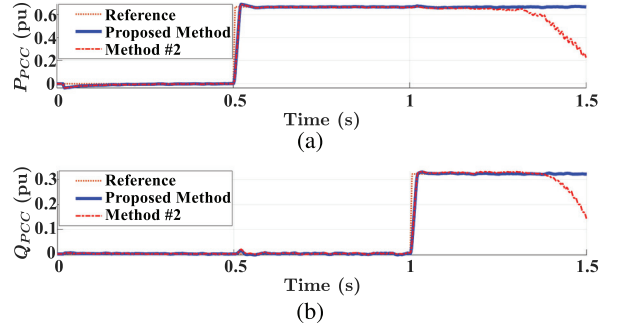


Fig. 13. Simulation of Fig. 3 connected to a balanced grid with high short-circuit capacity using Method #2 detailed in Section IV-B2. (a) Active power of  $P_{PCC}$  injected into PCC with/without FS. (b) Reactive power of  $Q_{PCC}$  injected into PCC with/without FS.

(53) insensitive to fault  $\mathbf{f}_{\text{FS}}$  exists for the augmented system if and only if the augmented system satisfies the following conditions: 1)  $\text{Rank}(\mathbf{C}_{\text{aug}} \mathbf{E}_{\text{aug}}) = \text{size}(\mathbf{f}_{\text{FS}})$ ; and 2) the invariant zeros (if exist) of  $(\mathbf{A}_{\text{aug}}, \mathbf{E}_{\text{aug}}, \mathbf{C}_{\text{aug}})$  are in the left-half-plane complex domain. Here,  $\mathbf{C}_{\text{aug}} \mathbf{E}_{\text{aug}} = \mathbf{A}_f \mathbf{E}$ .

The PI-based control structure with the sliding-mode-based fault observer described above has been employed in Fig. 3, whose parameters have been found in Table I. It has been simulated as detailed in Section IV-A1. The results of the test cases used in this research have been shown in Fig. 13(a)–(b). As they have shown, the system gets unstable because of the interactions between the observer and controller in the presence of the FSs made in this work. This instability problem could be anticipated because of the instability caused by the decoupling and feed-forward paths (as reported in [47]) since the fault observer fails to operate. Besides, it is not able to rectify the signals as there exist “no” adaptive dynamics to deal with the unknown upper bounds of the FSs. Indeed, this matter is combined with the instability issue induced by the decoupling and feed-forward paths introduced in [47].

### C. Proposed Approach's Experimental Results

A test rig has been used in order to conduct experimental evaluations of an *LCL*-filter-based GC-VSI. Fig. 14 shows the setup, which has the same parameters stated in Table I. It has been utilized to test the GC-VSI's performance when the GC-VSI is being exposed to FSs. The GC-VSI is based on intelligent power modules from SEMIKRON, including insulated gate bipolar transistors (IGBTs) built by “SKM 50 GB 123 D” modules, “SKHI 22 (AR)” gate drives, and protection circuitry. The switching frequency has been set to 8.1 kHz. The dc-link capacitance and inductance are 2.04 mF and 1.50 mH, respectively. The three-phase GC-VSI is operated at 30 A, 208 V (line-to-line rms), and 400 V (dc), which are all similar to the parameters employed in the simulations.

“IsoBlock I-ST-1c” current sensors and “IsoBlock V-1c” voltage sensors from Verivolt Company measure the currents and the voltages, respectively. “MicroLabBox (MLBX)” from dSPACE connects the GC-VSI under test to the measurement and drive printed circuit boards. A dual-core, 2 GHz “NXP (Freescale)

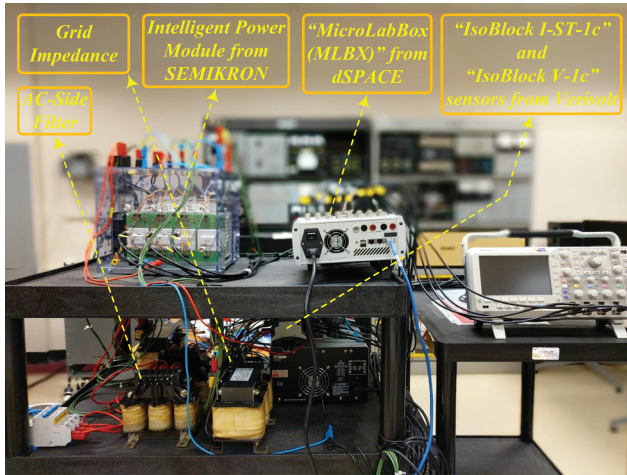


Fig. 14. Test rig used in the experiments.

QorIQ P5020™ real-time processor has executed and run the proposed control algorithm. “Xilinx Kintex-7 XC7K325T” field-programmable gate arrays (also known as FPGAs) have generated the PWM signals connected to digital inputs/outputs (I/Os). The MLBX interface board consists of eight 14-bit, 10 megasamples per second (Msps), differential analog-to-digital channels to interface the measured signals to the controller (with the functionality of free-running mode). The Real-Time-WorkShop in the MATLAB Simulink environment has generated the software code.

The same test cases as those in simulations in Section IV-A1 have been replicated here. As regards this matter, a similar test case—elaborated in Section IV-A1a—has been repeated here. Then, both active power and reactive power are first set to zero. Next, the reference signal of active power  $P_{\text{PCC}}$  is set to 0.6 pu. Then, while the other condition still exists, the reactive power  $Q_{\text{PCC}}$  is set to 0.3 pu. Fig. 15 is the counterpart of Fig. 5. It shows the emulated FSs, which are matched with those counterparts in simulations. Fig. 16 has shown the experimental results of the active/reactive power with FSs and its relevant references. In that figure, the actual active power, its reference, the actual reactive power, and its reference have been shown by traces in blue, magenta, cyan, and green, respectively, with 5.40 kW/div and 5.40 kvar/div, noted on the figure as well. Also, the V/div of each channel has been shown at the left-bottom corner for all variables in per unit (pu). Fig. 16(a) shows the whole snapshot of the experiments. Fig. 16(b) shows the experimental results associated with Fig. 6(a), and Fig. 16(c) demonstrate Fig. 6(b)’s counterpart in experiments. Last but not least, in order to check the performance of the proposed sliding-mode-based FS rectifier, an equivalent of Fig. 7 has been demonstrated in Fig. 17 with almost the same colors. In Fig. 17, FS to  $i_{2d}$ ,  $v_{cd}$ ,  $i_{2q}$ , and  $v_{cq}$  (all in pu) have been shown by traces in blue, cyan, magenta, and green, respectively—with 0.5 volts per division (V/div), also noted on the left-bottom corner of the figure. All pu bases are the  $y$ ’s arrays’ values of the GC-VSI’s operating point.

Simulations and experiments show good agreement with each other. In this regard, Figs. 5–7 are in excellent agreement with

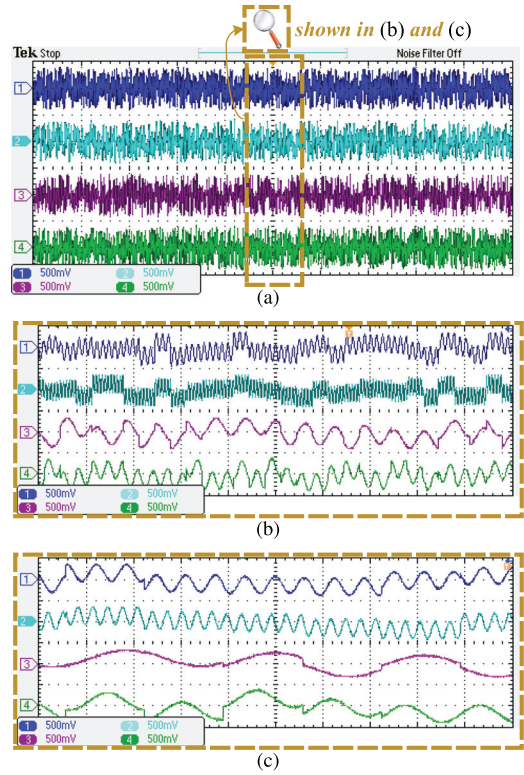


Fig. 15. Experimental results. (a) FS to  $i_{2d}$ ,  $i_{2q}$ ,  $v_{cd}$ , and  $v_{cq}$  [all in per unit (pu)] have been shown by traces in blue, cyan, magenta, and green, respectively, with 0.5 volts per division (V/div) noted at the left-bottom corner of the figure. (b) the enlarged view of Fig. 15(a) (with 100 ms/div). (c) Enlarged view of Fig. 15(a) (with 20 ms/div).

their equivalents, i.e., Figs. 15–17. Those consistent results reveal the effectiveness of the proposed faulty-signal-tolerant control for the GC-VSIs. Similarly—as shown in Figs. 16 and 17—the proposed FS rectifier is able to rectify the signals while embedded into the zero-level control and rigorously stabilize  $P_{\text{PCC}}$  and  $Q_{\text{PCC}}$ . Accordingly, if the used CPS cannot prevent something from coming into the zero-level control, the system is able to function by itself.

## V. CONCLUSION

As cyber threats necessitate us considering cybersecurity into systems from the beginning of the design process, this article has proposed a faulty-signal-tolerant control for PQ-controlled, grid-connected VSIs. It makes the grid-connected operation mode of VSIs more reliable for being employed in the modernized microgrids based on cyber-physical systems. The introduced controller is based on the sliding mode FS rectifier. As a result, it has provided a robust rectifier of FSs. Besides, the synthesized sliding-mode-based rectifier has an adaptation mechanism to take care of unknown bounds of the signals externally manipulated by FSs. Therefore, a new theory, including proof and other required mathematical analyses for the stability based on the Lyapunov criterion, has been presented. The proposed controller’s simulation results and experiments in

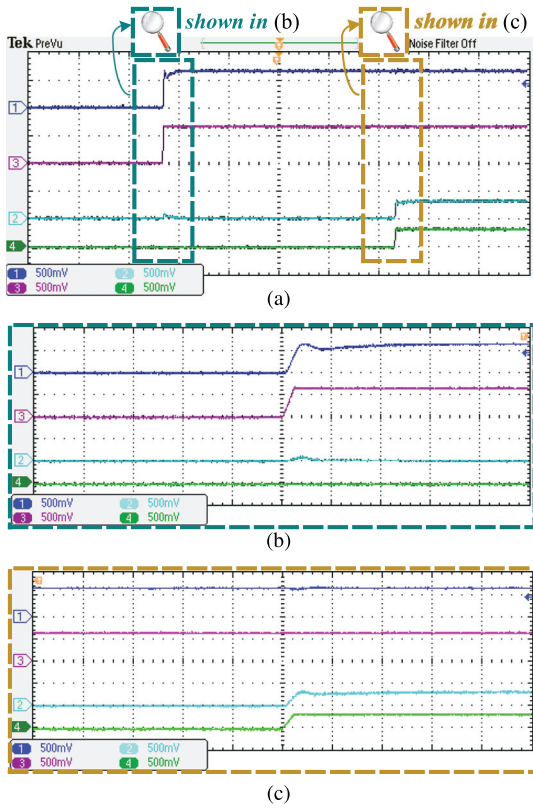


Fig. 16. Experimental results associated with active/reactive power changes. (a) Actual active power, its reference, the actual reactive power, and its reference have been shown by traces in blue, magenta, cyan, and green, respectively, with 5.40 kW/div and 5.40 kvar/div (their “pu” values have been noted at the left-bottom corner of the figures); and (b) and (a) are the enlarged views of Fig. 16(a)—with 25 ms/div—for both active power and reactive one.

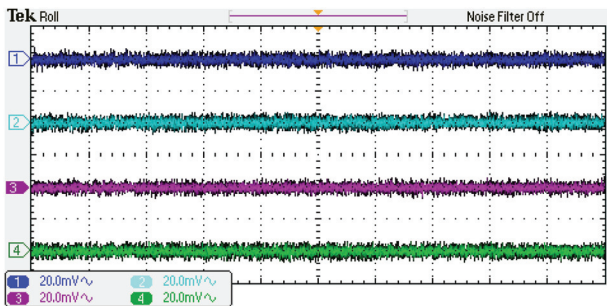


Fig. 17. Experimental results for the performance of the rectifier employed in generating Fig. 16.

the closed-loop system (when exposed to FSs virtually manipulating the outputs) have been displayed. They have revealed the effectiveness of the faulty-signal-tolerant control detailed in this research.

## REFERENCES

- [1] M. Davari, W. Gao, and F. Blaabjerg, “A fault-tolerant, passivity-based controller enhanced by the equilibrium-to-equilibrium maneuver capability for the DC-voltage power port VSC in multi-infeed AC/DC modernized grids,” *IEEE J. Emerg. Sel. Top. Power Electron.*, vol. 8, no. 3, pp. 2484–2507, Sep. 2020.
- [2] M. Davari, W. Gao, and F. Blaabjerg, “Analysing dynamics and synthesising a robust vector control for the dc-voltage power port based on the modular multilevel converter in multi-infeed AC/DC smart grids,” *IET Smart Grid*, vol. 2, no. 4, pp. 645–658, Dec. 2019.
- [3] R. Das, V. Madani, and A. P. S. Meliopoulos, “Leveraging smart grid technology and using microgrid as a vehicle to benefit DER integration,” in *Proc. IEEE Power Energy Soc. Innov. Smart Grid Technol. Conf.*, Apr. 2017, pp. 1–5.
- [4] *IEEE Application Guide for IEEE Std. 1547(TM), IEEE Standard for Interconnecting Distributed Resources With Electric Power Systems*, IEEE Std 1547.2-2008, Apr. 2009.
- [5] *Standard for Inverters, Converters, Controllers and Interconnection System Equipment for Use With Distributed Energy Resources*, UL1741 Standard, Jan. 2010.
- [6] M. Davari, W. Gao, Z.-P. Jiang, and F. L. Lewis, “An optimal primary frequency control based on adaptive dynamic programming for islanded modernized microgrids,” *IEEE Trans. Autom. Sci. Eng.*, to be published, doi: [10.1109/TASE.2020.2996160](https://doi.org/10.1109/TASE.2020.2996160).
- [7] J. Shiles *et al.*, “Microgrid protection: An overview of protection strategies in North American microgrid projects,” in *Proc. IEEE-PES General Meeting*, Jul. 2017, pp. 1–5.
- [8] I. U. Nutkani, L. Meegahapola, P. C. Loh, and F. Blaabjerg, “Autonomous power management for interlinked AC-DC microgrids,” *CSEE J. Power Energy Syst.*, vol. 4, no. 1, pp. 11–18, Mar. 2018.
- [9] S. H. Mousavi, M. Davari, and H. J. Marquez, “An innovative event-based filtering scheme using  $H_\infty$  performance for stochastic LTI systems considering a practical application in smart modernized microgrids,” *IEEE Access*, vol. 7, pp. 48 138–48 150, Apr. 2019.
- [10] S. Sridhar, A. Hahn, and M. Govindarasu, “Cyber-physical system security for the electric power grid,” *Proc. IEEE*, vol. 1, no. 100, pp. 210–224, Jan. 2012.
- [11] K. Tehrani, “A smart cyber physical multi-source energy system for an electric vehicle prototype,” *J. Syst. Architecture*, vol. 111, Jun. 2020, Art. no. 101804.
- [12] B. Tang, “Toward intelligent cyber-physical systems: Algorithms, architectures, and applications,” Ph. D. thesis, Dept. Elect., Comput., Biomed. Eng., Univ. Rhode Island, Kingston, RI, USA, 2016. [Online]. Available: [https://digitalcommons.uri.edu/oa\\_diss/481](https://digitalcommons.uri.edu/oa_diss/481)
- [13] Y. Yuan *et al.*, “Data driven discovery of cyber physical systems,” *Nature Commun.*, vol. 10, Oct. 2019, Art. no. 4894.
- [14] G. Spezzano and A. Vinci, “Pattern detection in cyber-physical systems,” *Procedia Comput. Sci.*, vol. 52, pp. 1016–1021, 2015.
- [15] H. Ye, Q. Mou, X. Wang, and Y. Liu, “Eigen-analysis of large delayed cyber-physical power system by time integration-based solution operator discretization methods,” *IEEE Trans. Power Syst.*, vol. 33, no. 6, pp. 5968–5978, Nov. 2018.
- [16] Z. Qu *et al.*, “Power cyber-physical system risk area prediction using dependent Markov chain and improved grey wolf optimization,” *IEEE Access*, vol. 8, pp. 82 844–82 854, May 2020.
- [17] H. Ye, Q. Mou, and Y. Liu, “Calculation of critical oscillation modes for large delayed cyber-physical power system using pseudo-spectral discretization of solution operator,” *IEEE Trans. Power Syst.*, vol. 32, no. 6, pp. 4464–4476, Nov. 2017.
- [18] X. Liu, C. Qian, W. G. Hatcher, H. Xu, W. Liao, and W. Yu, “Secure internet of things (IoT)-based smart-world critical infrastructures: Survey, case study and research opportunities,” *IEEE Access*, vol. 7, pp. 79 523–79 544, Jun. 2019.
- [19] S. Zuo, O. A. Beg, F. L. Lewis, and A. Davoudi, “Resilient networked AC microgrids under unbounded cyber attacks,” *IEEE Trans. Smart Grid*, vol. 11, no. 5, pp. 3785–3794, Sep. 2020.
- [20] M. G. Angle, S. Madnick, J. L. Kirtley, and S. Khan, “Identifying and anticipating cyberattacks that could cause physical damage to industrial control systems,” *IEEE Power Energy Technol. Syst. J.*, vol. 6, no. 4, pp. 172–182, Dec. 2019.
- [21] S. Gholami, S. Saha, and M. Aldeen, “Fault tolerant control of electronically coupled distributed energy resources in microgrid systems,” *Int. J. Elect. Power Energy Syst.*, vol. 95, pp. 327–340, Feb. 2018.
- [22] A. A. Cárdenas, S. Amin, and S. Sastry, “Secure control: Towards survivable cyber-physical systems,” in *Proc. 28th Int. Conf. Distrib. Comput. Syst. Workshops*, Jun. 2008, pp. 495–500.
- [23] S. Sahoo, T. Dragičević, and F. Blaabjerg, “Cyber security in control of grid-tied power electronic converters—challenges and vulnerabilities,” *IEEE J. Emerg. Sel. Top. Power Electron.*, to be published, doi: [10.1109/JESTPE.2019.2953480](https://doi.org/10.1109/JESTPE.2019.2953480).

[24] S. Sahoo, Y. Yang, and F. Blaabjerg, "Resilient synchronization strategy for AC microgrids under cyber attacks," *IEEE Trans. Power Electron.*, vol. 36, no. 1, pp. 73–77, Jan. 2021.

[25] X. Li, Q. Xu, and F. Blaabjerg, "Adaptive resilient secondary control for islanded AC microgrids with sensor faults," *IEEE J. Emerg. Sel. Top. Power Electron.*, to be published, doi: 10.1109/JESTPE.2020.2988509.

[26] J. C. Balda, A. Mantooth, R. Blum, and P. Tenti, "Cybersecurity and power electronics: Addressing the security vulnerabilities of the internet of things," *IEEE Power Electron. Mag.*, vol. 4, no. 4, pp. 37–43, Dec. 2017.

[27] A. Sivanathan, H. H. Gharakheili, and V. Sivaraman, "Managing IoT cyber-security using programmable telemetry and machine learning," *IEEE Trans. Netw. Service Manage.*, vol. 17, no. 1, pp. 60–74, Mar. 2020.

[28] N. Young and R. Drees, "Cyber security for automatic test equipment," *IEEE Instrum. Meas. Mag.*, vol. 21, no. 4, pp. 4–8, Aug. 2018.

[29] X. He, R. Gamble, and M. Papa, "A smart contract grammar to protect IoT firmware updates using hyperledger fabric," in *Proc. IEEE 10th Annu. Inf. Technol., Electron. Mobile Commun. Conf.*, Oct. 2019, pp. 34–42.

[30] C. Glenn, D. Sterbentz, and A. Wright, "Cyber threat and vulnerability analysis of the U.S. electric sector," Idaho Nat. Lab. (Mission Support Center), Idaho Falls, ID, USA, Tech. Rep. INL/EXT-16-40692, Aug. 2016.

[31] D. I. Dogaru and I. Dumitache, "Robustness of power systems in the context of cyber attacks," in *Proc. 21st Int. Conf. Control Syst. Comput. Sci.*, Jul. 2017, pp. 506–512.

[32] J. Qi, A. Hahn, X. Lu, J. Wang, and C.-C. Liu, "Cybersecurity for distributed energy resources and smart inverters," *IET Cyber-Physical Syst.: Theory Appl.*, vol. 1, no. 1, pp. 28–39.

[33] K. Horowitz *et al.*, "A guidebook for distributed energy resource (DER) interconnection," Nat. Renewable Energy Lab.(NREL), Tech. Rep. NREL/TP-6A20-72102, Apr. 2019.

[34] R. Nuqui, "Cyberattack resilient HVDC system (CARDS)," Cybersecurity for Energy Delivery Systems (CEDS), U.S. Dept. Energy, Washington, DC, USA, 2018. [Online]. Available: <https://www.energy.gov/sites/prod/files/2018/12/f58/ABB - Cyber Attack Resilient HVDC System.pdf>

[35] Congressional Research Service, "Cybersecurity for energy delivery systems: DOE programs," U.S. Dept. Energy, Washington, DC, USA, Tech. Rep. R44939, [Online]. Available: <https://crsreports.congress.gov/product/pdf/R/R44939>

[36] L. Slotine and W. Li, "Advanced stability theory," in *Applied Nonlinear Control*. Englewood Cliffs, NJ, USA: Prentice Hall, 1991, ch. 4, pp. 123–126, Section 4.5.2.

[37] M. P. Aghababa and M. Saif, "Adaptive control realization for canonic Caputo fractional-order systems with actuator nonlinearity: Application to mechatronic devices," *Adv. Difference Equ.*, Jul. 2020, Art. no. 372.

[38] V. Utkin, J. Guldner, and J. Shi, "The Chattering Problem" in *Sliding Mode Control in Electro-Mechanical Systems*, 2nd ed. Boca Raton, FL, USA: CRC Press, 2009, ch. 8.

[39] H. Brandstädter, "Sliding mode control of electromechanical systems," Ph.D. dissertation, Fac. Elect. Eng. Inf. Technol., Tech. Univ. Munich, Munich, Germany, Mar. 2009. [Online]. Available: <https://mediatum.ub.tum.de/doc/667446/667446.pdf>

[40] M. Davari, M. P. Aghababa, F. Blaabjerg, and M. Saif, "A modular adaptive robust nonlinear control for resilient integration of VSIs into emerging modernized microgrids," *IEEE J. Emerg. Sel. Top. Power Electron.*, to be published, doi: 10.1109/JESTPE.2020.2984231.

[41] A. Aghazadeh, M. Davari, H. Nafisi, and F. Blaabjerg, "Grid integration of a dual two-level voltage-source inverter considering grid impedance and phase-locked loop," *IEEE J. Emerg. Sel. Top. Power Electron.*, to be published, doi: 10.1109/JESTPE.2019.2953522.

[42] H.-S. Song and K. Nam, "Dual current control scheme for PWM converter under unbalanced input voltage conditions," *IEEE Trans. Ind. Electron.*, vol. 46, no. 5, pp. 953–959, Oct. 1999.

[43] M. Davari and Y. A.-R. Mohamed, "Robust vector control of a very weak-grid-connected voltage-source converter considering the phase-locked loop dynamics," *IEEE Trans. Power Electron.*, vol. 32, no. 2, pp. 977–994, Feb. 2017.

[44] C. Edwards, S. K. Spurgeon, and C. P. Tan, "On the development and application of sliding mode observers," in *Variable Structure Systems: Towards the 21st Century. Lecture Notes in Control and Information Sciences*. X. Yu and J.-X. Xu, Eds. Berlin, Heidelberg: Springer, 2002, vol. 274, pp. 253–282.

[45] C. Tan and C. Edwards, "Sliding mode observers for detection and reconstruction of sensor faults," *Automatica*, vol. 38, no. 10, pp. 1815–1821, 2002.

[46] C. Pin and T. C. Edwards, "Sliding mode observers for robust fault detection & reconstruction," *IFAC Proc. Volumes*, vol. 35, no. 1, pp. 347–352, 2002.

[47] S. Silwal, M. Karimi-Ghartemani, R. Sharma, and H. Karimi, "Impact of feed-forward and decoupling terms on stability of grid-connected inverters," in *Proc. IEEE 28th Int. Symp. Ind. Electron.*, Jun. 2019, pp. 2641–2646.



**Masoud Davari** (Senior Member, IEEE) was born in Isfahan, Iran, on Sep. 14, 1985. He received the B.Sc. degree (with distinction) in electrical engineering-power from the Isfahan University of Technology, Isfahan, Iran, in Sep. 2007, the M.Sc. degree (with distinction) in electrical engineering-power from the Amirkabir University of Technology (Tehran Polytechnic), Tehran, Iran, in 2010, and the Ph.D. degree in electrical engineering-energy systems from the Univ. Alberta, Edmonton, AB, Canada, in 2016.

He was with Iran's Grid Secure Operation Research Center and Iran's Electric Power Research Institute (EPRI) in Tehran, Iran, from January 2010 to December 2011. From April 2015 to June 2017, he has been collaborating with Quanta-Technology Company, Markham, ON, Canada, in the field of the dynamic interaction of renewable energy systems with smart grids as well as control, protection, and automation of microgrids as a Senior R&D Specialist and Senior Consultant. In July 2017, he joined the Department of Electrical and Computer Engineering in Allen E. Paulson College of Engineering and Computing at Georgia Southern University, Statesboro, GA, USA, as a tenure-track Assistant Professor. He is the Founder and Director of the Laboratory for Advanced Power and Energy Systems (LAPES) in the state-of-the-art Center for Engineering and Research (CEaR) established in 2021 at Georgia Southern University. He has developed and implemented several experimental test rigs for both research universities and the industry. He has also authored several IEEE Transactions and Journals. His research interests include the dynamics, controls, and protections of different types of power electronic converters, which are utilized in the hybrid ac/dc smart grids, and hardware-in-the-loop (HIL) testing of modernized power systems.

Dr. Davari serves as an active member and a Chapter Lead (for Chapter 3) in the IEEE WG P2004, a newly established IEEE working group on the HIL simulation for IEEE Standards Association, from June 2017 until now. He is an invited member of the Golden Key International Honour Society. He served as the Chair of the Literature Review Subgroup of DC@home Standards for the IEEE Standards Association from April 2014 to October 2015. He is an invited reviewer of several of the IEEE TRANSACTIONS and Journals, IET journals, *Energies* Journal, and various IEEE conferences, as well as the invited speaker at different universities and in diverse societies and the Best Reviewer of the IEEE TRANSACTIONS ON POWER SYSTEMS in 2018. He was the recipient of the Allen E. Paulson College of Engineering and Computing (CEC) Faculty Award for Scholarly Activity in the Allen E. Paulson CEC at Georgia Southern University from 2019 to 2020.



**Mohammad Pourmahmood Aghababa** (Member, IEEE) was born in Tabriz, Iran, in 1983. He received the Ph.D. degree in electrical engineering (major control engineering) from the University of Tabriz, Tabriz, Iran, in 2011.

He is currently a Professor with the Urmia University of Technology, Urmia, Iran, and a Researcher with the University of Windsor, Windsor, ON, Canada. Before joining the University of Windsor, he was a Researcher with the École Centrale de Nantes, Nantes, France. He has authored or coauthored over 90 international ISI-JCR journal articles. He has also authored a book entitled "Advanced Nonlinear Control Systems: Theory, Design and Applications" (in Persian). His current research interests include control theory and application, robotics and mechatronics, machine learning and AI, and fractional-order systems.

Dr. Aghababa has served as a Technical Committee Member for many international conferences. He was recognized as the Youngest Full Professor among all the universities of the Ministry of Science, Research and Technology of Iran, in 2018. He has been nominated as one of the best one percent highly cited researchers of the world in the engineering field from 2017 to 2020. He is an Associate Editor for the *International Journal of Machine Learning and Cybernetics* and the *Journal of Control, Automation and Electrical Systems*.



**Frede Blaabjerg** (Fellow, IEEE) received the Ph.D. degree in electrical engineering from Aalborg University, Aalborg, Denmark, in 1995, and the honoris causa degree from the University Politehnica Timisoara (UPT), Timisoara, Romania, in 2017, and Tallinn Technical University (TTU), Tallinn, Estonia, in 2018.

He was with ABB-Scandia, Randers, Denmark, from 1987 to 1988. He became an Assistant Professor with the Department of Energy Technology, Aalborg University, Aalborg, Denmark, in 1992, an Associate Professor in 1996, and a Full Professor of power electronics and drives, in 1998, where he has been a Villum Investigator, since 2017. He has authored or coauthored more than 600 journal articles in different fields of power electronics and its applications, coauthored four monographs, and edited ten books in power electronics and its applications. He was nominated by Thomson Reuters to be included in the 250 most cited researchers in engineering in the world in 2014–2018. His current research interests include power electronics and its applications, such as in wind turbines, photovoltaic systems, reliability, harmonics, and adjustable speed drives.

Dr. Blaabjerg was the recipient of the 31 IEEE Prize Paper Awards, the IEEE PELS Distinguished Service Award, in 2009, the EPE-PEMC Council Award, in 2010, the IEEE William E. Newell Power Electronics Award, 2014, and the Villum Kann Rasmussen Research Award, 2014. He was a recipient of the Global Energy Award for a significant contribution to the development of technologies that provide new energy development opportunities, in 2019. He was a recipient of the IEEE Edison Medal, in 2020. He was the Editor-in-Chief for the IEEE TRANSACTIONS ON POWER ELECTRONICS, from 2006 to 2012. He was a Distinguished Lecturer of the IEEE Power Electronics Society, from 2005 to 2007, and the IEEE Industry Applications Society, from 2010 to 2011 and 2017 to 2018. He is the President of the IEEE Power Electronics Society for 2019–2020 and the Vice President of the Danish Academy of Technical Sciences.



**Mehrdad Saif** (Senior Member, IEEE) received the B.S.E.E., M.S.E.E., and D.Eng. degrees from Cleveland State University, Cleveland, OH, USA, in 1982, 1984, and 1987, respectively.

During his graduate studies, he worked on research projects sponsored by the Cleveland Advanced Manufacturing Program, National Aeronautics and Space Administration (NASA) Glenn Research Center, Cleveland, OH, USA. In 1987, he joined as an Assistant Professor with the School of Engineering Science, Simon Fraser University, Burnaby, BC, Canada,

where he was the Director of the School of Engineering Science from 2002 to 2011 and led a major expansion of that school during his term. He has been the Dean of the Faculty of Engineering, University of Windsor, Windsor, ON, Canada, since 2011. In this role, he has led significant enrolment growth through strategic enrolment management and the expansion of the Faculty of Engineering programs into areas, such as aerospace engineering, engineering management, B.Eng. technology, mechatronics, and others. He has also overseen significant growth in the number of faculty and research productivity of the Faculty of Engineering. He has been a Consultant to a number of industries and agencies, such as General Motors, Detroit, MI, USA, NASA, Washington, DC, USA, BC Hydro, Vancouver, BC, Canada, Ontario Council of Graduate Studies, Toronto, ON, Canada, and others. He has authored or coauthored over 350 refereed journal and conference articles and edited a book in the areas of his interests. His research interests include systems and control, estimation and observer theory, model-based fault diagnostics, condition monitoring, diagnostics and prognostic, and application of these areas to automotive, power, autonomous systems, and other complex and cyber-physical systems.

Dr. Saif is a fellow of the Canadian Academy of Engineering and the Institution of Engineering and Technology. He is a Registered Professional Engineer in Ontario, Canada. He is currently a member of the Editorial Board of IEEE ACCESS and the IEEE SYSTEM JOURNAL. He served as the Chairman of the Vancouver Section of the IEEE Control Systems Society, in 1995 and 1997.